Impact of Variable Atmospheric and Oceanic Form Drag on Simulations of Arctic Sea Ice*

MICHEL TSAMADOS, DANIEL L. FELTHAM, DAVID SCHROEDER, AND DANIELA FLOCCO

Centre for Polar Observation and Modelling, Department of Meteorology, University of Reading, Reading, United Kingdom

SINEAD L. FARRELL

Earth System Science Interdisciplinary Center, University of Maryland, College Park, College Park, Maryland

NATHAN KURTZ

Goddard Earth Science Technology and Research Program, Mergan State University, Baltimore, Maryland

SEYMOUR W. LAXON+

Centre for Polar Observation and Modelling, University College London, London, United Kingdom

SHELDON BACON

National Oceanography Center, University of Southampton, Southampton, United Kingdom

(Manuscript received 2 October 2013, in final form 12 December 2013)

ABSTRACT

Over Arctic sea ice, pressure ridges and floe and melt pond edges all introduce discrete obstructions to the flow of air or water past the ice and are a source of form drag. In current climate models form drag is only accounted for by tuning the air–ice and ice–ocean drag coefficients, that is, by effectively altering the roughness length in a surface drag parameterization. The existing approach of the skin drag parameter tuning is poorly constrained by observations and fails to describe correctly the physics associated with the air–ice and ocean–ice drag. Here, the authors combine recent theoretical developments to deduce the total neutral form drag coefficients from properties of the ice cover such as ice concentration, vertical extent and area of the ridges, freeboard and floe draft, and the size of floes and melt ponds. The drag coefficients are incorporated into the Los Alamos Sea Ice Model (CICE) and show the influence of the new drag parameterization on the motion and state of the ice cover, with the most noticeable being a depletion of sea ice over the west boundary of the Arctic Ocean and over the Beaufort Sea. The new parameterization allows the drag coefficients to be coupled to the sea ice state and therefore to evolve spatially and temporally. It is found that the range of values predicted for the drag coefficients agree with the range of values measured in several regions of the Arctic. Finally, the implications of the new form drag formulation for the spinup or spindown of the Arctic Ocean are discussed.

1. Introduction

Arctic sea ice, after more than three decades of prolonged thinning and shrinking, has transformed radically with a large increase of first-year ice and an almost total disappearance of older (more than 5 years) multiyear ice (Stroeve et al. 2012). With this evolution comes the necessity to reevaluate the physical processes involving

* Supplemental information related to this paper is available at the Journals Online website.

+ Deceased.

Corresponding author address: Michel Tsamados, Centre for Polar Observation and Modelling, Department of Meteorology, University of Reading, Reading, RG6 6BB, United Kingdom.
E-mail: m.c.tsamados@rdg.ac.uk

DOI: 10.1175/JPO-D-13-0215.1

sea ice and, in particular, the driving mechanisms that set the ice in motion and redistribute its mass into and out of the Arctic Basin. Usually three forces dominate in the momentum balance of sea ice: the atmospheric drag, the oceanic drag, and the internal forces in the ice. While understanding the mechanical properties and rheology of sea ice remains an active domain of research (Coon et al. 2007; Feltham 2008; Tsamados et al. 2013), the aim of this paper is to address the fluxes of momentum (also called drag) between the air and the ice and between the ocean and the ice.

Over heterogeneous surfaces these turbulent fluxes can be calculated by two different methods (Claussen 1990; Vihma 1995): flux aggregation or parameter aggregation. Here the flux aggregation method is applied over sea ice; fluxes are determined for the ice-covered area and for the open water area and the various fluxes are then combined, according to their relative associated areas. The turbulent surface fluxes of momentum (or drag) $\boldsymbol{\tau}$, sensible heat H, and latent heat LE over sea ice are commonly expressed as

$$\boldsymbol{\tau} = \rho C_d(z) U(z) [\cos\theta \mathbf{U}(z) + \sin\theta \mathbf{k} \times \mathbf{U}(z)], \quad (1)$$

$$H = \rho c_p C_H(z)(\theta_s - \theta_z) U(z), \quad (2)$$

and

$$\mathrm{LE} = \rho \gamma C_E(z)(q_s - q_z) U(z), \quad (3)$$

where $\mathbf{k}$ is the vertical unit vector, ρ is the air (water) density, c_p is the specific heat of air (water), γ is the latent heat of vaporization, $\mathbf{U}(z)$ is the difference in air (water) and ice velocity at height z above (below) sea level, $U(z) = |\mathbf{U}(z)|$, θ is a turning angle, and $\theta_s - \theta_z$ and $q_s - q_z$ are the differences in potential temperature and specific humidity, respectively, between the surface s and at height z. (See Table 1 for a list of notation used throughout the manuscript.)

While Eq. (1) is currently used in most sea ice models (Hibler 1979; Hunke 2010), McPhee (2012) suggests deviating from this quadratic drag relationship and uses a Rossby similarity approach that better accounts for the dependence on $\mathbf{U}(z)$ of the drag and turning angle. McPhee (2012) also recommends generalizing the treatment of the ice–ocean stress to account for buoyancy effects and for the strength and depth of the pycnocline. Because the focus of this paper is on estimating the form drag contribution and its dependence on the sea ice characteristics, we want to keep the treatment of the drag as simple as possible and therefore keep the treatment of Eq. (1). We also assume a constant turning angle (zero in this paper) and treat atmospheric and oceanic drag as analogous with logarithmic velocity profiles near the ice.

The transfer coefficients for momentum $C_d(z)$, sensible heat $C_H(z)$, and latent heat $C_E(z)$ can be determined using the Monin–Obukhov similarity theory as functions of the roughness length z_0 and universal stability functions [see, e.g., Schröder et al. (2003) for details]. The three transfer coefficients are proportional and one therefore expects that the surface heat and momentum transfers are correlated. Here we keep the default Los Alamos Sea Ice Model (CICE) assumption (Hunke and Lipscomb 2010) that all neutral transfer coefficients are equal [for the limit of validity of this assumption see Schröder et al. (2003)]. We leave the sensitivity study of the model to the heat transfer coefficients for future investigation. Schröder et al. (2003) describe the methods used to measure the transfer coefficients experimentally and report values of these coefficients for the atmosphere–ice interface over various regions of the Arctic.

In this paper we describe the impact of form drag on the neutral drag coefficient, that is, for a neutral stratification of the ambient fluid (Stull 1988). However, the drag coefficients can vary widely depending on atmospheric (and oceanic) stability (Birnbaum and Lüpkes 2002) and are known to be strongly enhanced (reduced) in an unstable (stable) boundary layer where strong (weak) turbulent mixing is present. Hereafter, drag coefficient always refers to the neutral drag coefficient unless explicitly stated. As first noted by Arya (1973), the total neutral drag can be decomposed into the skin frictional or viscous drag that acts on much of the level undeformed surface and the form drag that acts on hummocks, pressure sails, keels, and floe or melt pond edges.

Most current climate or sea ice models encompass a simple parameterization of the skin drag with a square drag law and a constant drag coefficient to model air–ice and ice–ocean stresses (Hibler 1979). Some exceptions (Tremblay and Mysak 1997; Steiner et al. 1999) have incorporated a form drag term that depends on the sea ice characteristics (thickness and mechanical properties) and have shown a potential to influence to a large degree the redistribution and export of the ice over the Arctic Basin. Direct numerical simulations (Leonardi et al. 2003; Le et al. 1997) of the turbulent flow over regularly spaced obstacles typical of the winter pack ice, where the sails and keel density are large, confirm Arya's prediction (Arya 1973) that the form drag term can become the dominant contribution to the total drag for both the ocean and atmospheric drag. In the marginal ice zone (MIZ), on the other hand, estimates from Hanssen-Bauer and Gjessing (1988), Steele et al. (1989), Mai et al. (1996), and Lu et al. (2011) have shown that in low concentration sea ice regions the contribution of form drag due to the floe edges can also exceed the

TABLE 1. Notation.

α,β	Weight functions
α_k	Keel slope
α_r	Sail slope
$\boldsymbol{\tau}$	Momentum flux (drag)
$\mathbf{U}(z)$	Fluid speed at height
γ	Latent heat of vaporization
ϕ_k	Porosity of the keels
ϕ_s	Porosities of the sails
ρ_a	Air density
ρ_i	Ice density
ρ_s	Snow density
ρ_w	Water density
θ	Potential temperature
A^*	Cutoff ice concentration to avoid singularity
a_i	Ice concentration in CICE
a_{lvl}	Level ice concentration in CICE
A_p	Pond concentration
a_{rdg}	Ridged ice concentration in CICE
c	Coefficient of resistance of an individual obstacle
c_p	Specific heat of air
C_{daf}	Form drag contribution from floe edge freeboard
C_{dap}	Form drag contribution from melt pond edges
C_{dar}	Form drag contribution from sails
C_{das}	Surface skin drag contribution
C_{da}	Total atmospheric drag coefficient
$C_{\mathrm{da}}^{\mathrm{SKIN}}$	Reference atmospheric neutral drag coefficient
C_{dwf}	Form drag contribution from floe edge draft
C_{dwr}	Form drag contribution from keels
C_{dws}	Bottom surface skin drag contribution
C_{dw}	Total oceanic drag coefficient
c_{dw}	Local coefficient of resistance at the floe edge
$C_{\mathrm{dw}}^{\mathrm{SKIN}}$	Reference oceanic neutral drag coefficient
C_E	Transfer coefficient for latent heat
c_{fa}	Local coefficient of resistance at the floe edge
C_H	Transfer coefficient for sensible heat
c_{kw}	Local coefficient of resistance of a keel
c_{pa}	Local coefficient of resistance at the pond edge
c_{sa}	Unobstructed skin drag
c_{ra}	Local coefficient of resistance of a sail
c_{sf}	Geometrical parameter associated with the floe shape
c_{sp}	Geometrical parameter associated with the pond shape
c_{sw}	Unobstructed skin drag
D	Distance between obstacles
D	Draft at the floe edge
D_f	Average distance between floes
D_k	Average distance between keels
D_s	Average distance between sails
f	Force per unit upstream frontal area of N obstacles
g	Geometrical factor accounting for the orientation of the obstacles
H	Height of one obstacle
H	Sensible heat flux
H_p	Freeboard of the melt ponds
H_s	Snow thickness
H_f	Freeboard at the floe edge
H_k	Average keel depth
H_s	Average sail height
L	Average floe size
L_x	Grid cell width
L_y	Grid cell width
L_y	Transverse length of one obstacle
L_{max}	Max floe size
L_{min}	Min floe size
$L_{p_{\mathrm{max}}}$	Max pond size
$L_{p_{\mathrm{min}}}$	Min pond size
LE	Latent heat flux
m_a	Skin drag attenuation parameter
m_w	Skin drag attenuation parameter
N	Number of obstacles in the reference domain
P	Average dynamic pressure per obstacle
q	Specific humidity
R_d	Ratio of D_k over D_s
R_h	Ratio of H_k over H_s
S_c	Sheltering function
s_l	Attenuation parameter
S_T	Surface area of the reference domain/grid cell area
V_k	Volume of one keel
v_{lvl}	Grid cell level ice average thickness in CICE
v_{rdg}	Grid cell ridged ice average thickness in CICE
V_r	Volume of one sail
X_k	Keel width
X_r	Sail width
z_0	Roughness length of the upstream surface type
z_{0i}	Roughness length of level ice
z_{0w}	Roughness length of water upstream of the floe
z_a	Ice surface roughness length
z_w	Bottom surface ice roughness length

skin frictional drag. Finally, it was recently argued that during the melt season melt pond edges could contribute to the rise in the measured total atmospheric neutral drag coefficient (Andreas et al. 2010; Lüpkes et al. 2012, 2013).

The dependence of the atmospheric neutral drag coefficient (ANDC) and oceanic neutral drag coefficient (ONDC) on the ice characteristics is confirmed by measurements of these coefficients over different regions of the Arctic, over different ice types, and during different seasons of the year. While direct flux measurements over the broken, heterogeneous Arctic sea ice surface are rare, particularly at the ice–ocean interface, measurements show a strong spatial and temporal variability with increased ANDC (Schröder et al. 2003) and ONDC (Lu et al. 2011) for multiyear ice in heavily ridged regions at the western (meaning west of the Greenwich meridian) Arctic Ocean boundary or for regions with low sea ice concentration (e.g., in the MIZ). More recently, Andreas et al. (2010) reported a marked increase in the ANDC over summer sea ice (associated with an increased form drag contribution from the floe and melt pond edges).

The sea ice geometry parameters relevant to form drag parameterization over sea ice have been inferred from observations. As reviewed in Martin (2007), statistical information of the height and frequency of sails and keels can be obtained over a large part of the Arctic Basin with a combination of laser airborne instruments such

as laser altimeters (Farrell et al. 2012), electromagnetic birds (Haas 2004) and upward-looking sonar instruments attached to moorings (Melling et al. 1995; Fissel et al. 2004), submarines (Wadhams and Davy 1986), or autonomous underwater vehicles (Wadhams et al. 2004). On the other hand, because of their inherently two-dimensional nature, statistical information on floe and melt pond size and spacing can more easily be retrieved from high-resolution satellite imagery (Weiss and Marsan 2004; Lüpkes et al. 2012).

In section 2, we introduce the parameterizations for both the atmosphere–ice and ocean–ice drag contributions. We decompose the ANDC into its skin drag and form drag, the latter containing the sail, floe edge, and melt pond edge contributions, and we decompose the ONDC into its skin drag and form drag, the latter containing the keel and floe edge contributions. In section 3, we briefly present the setup of the sea ice climate component CICE used in this work and describe the procedure that is used to implement the new parameterizations into the model. In section 4, we describe the impact of the new parameterization scheme on the Arctic sea ice characteristics of a model reference run. We then proceed, in section 5, to a sensitivity study of the new Arctic simulations to uncertain parameters in the drag formulations. Finally, in section 6, we summarize our results.

2. Drag parameterizations

a. *General formulation of form drag on randomly oriented obstacles*

Arya (1973) defined the drag force per unit length of a sail of height H, oriented normal to the flow, for a flow speed of $U(H)$ at height H, as $f_D = Hc[\rho U(H)^2/2]$, where c is the coefficient of resistance of the individual obstacle [for typical values of c over sea ice, see Garbrecht et al. (1999)]. Hanssen-Bauer and Gjessing (1988) later introduced a similar expression for f_D where the squared fluid flow profile is integrated over the entire obstacle height. To treat the more general case where the fluid flow is obstructed by an ensemble of asperities, we assume that N discrete obstacles of height H and transverse length L_y are spatially distributed on a domain of surface area S_T. At this stage we make no assumption as to the type of obstacle, which could be a keel, sail, floe, or melt pond edge. Similarly we do not distinguish between the flowing fluid, which could be either the atmosphere or the ocean. Following Lüpkes et al. (2012), we determine as a first step the average dynamic pressure per obstacle P, defined as the force f per unit frontal upstream area of the N obstacles as

$$P = \frac{f}{NHL_y}, \tag{4}$$

with f defined by the integral

$$f = NS_c^2 L_y g \int_{z_0}^{H} c\frac{\rho U^2}{2} dz, \tag{5}$$

where z_0 is a roughness length, U is the height-dependent upstream fluid speed, and S_c is the sheltering function for the obstacle considered that will depend on the typical distance between obstacles D and on their height H. Here the sheltering function is considered independent of the fluid speed and height. In Eq. (5), g is a geometrical factor that depends on the shape of the obstacle. For example, for linear obstacles (sail, keels, and floe edges) with a uniform distribution of orientations this factor should be $g = \int_{-\pi/2}^{\pi/2} 1/\pi \cos\theta \, d\theta = 2/\pi$, where θ is the angle between the normal to the obstacle and the flow direction and the integral represents an average over all orientations of the obstacles. Then, τ, the magnitude of the momentum flux per unit area of the domain or drag force acting on the domain area S_T, is given by

$$\tau S_T = PNL_y H. \tag{6}$$

The associated effective neutral 10-m drag coefficient can be deduced from

$$C_d(10) = \frac{\tau}{\rho U(10)^2}. \tag{7}$$

From now on we will implicitly assume that the drag coefficient is measured at 10 m and will drop the functional dependence. As described by Hanssen-Bauer and Gjessing (1988), assuming a logarithmic fluid velocity profile $U = (u_\star/\kappa)\ln(z/z_0)$ (κ is the von Kármán constant), one can integrate Eq. (5), and in combination with Eqs. (4), (6), and (7) one can write the general form drag coefficient:

$$C_d = \frac{NcS_c^2 g L_y H}{2S_T}\left[\frac{\ln(H/z_0)}{\ln(10/z_0)}\right]^2, \tag{8}$$

where we have used the simplification $[\ln(H/z_0 e)]^2 + 1 - 2z_0/H \simeq [\ln(H/z_0)]^2$, which is justified to within 1% relative error for typical values of H and z_0. Note that this corresponds to Arya's simplification to consider the fluid velocity simply at the height H instead of integrating over H, as in Eq. (5). In the literature, the z_0 is chosen to be the roughness length of the upstream surface type. Direct numerical simulations (Leonardi et al. 2003) have shown that for low enough ratios of obstacle height over the distance between obstacles H/D, the

parameter z_0 should be replaced by a displacement height d_0 that has a monotonic decreasing functional dependence on H/D. Note that the term in the bracket in Eq. (8) varies little with H and z_0 and can be incorporated, in a first approximation, in the coefficient of resistance c. In Eqs. (5) and (8), in line with the literature, this effect is instead accounted for by the phenomenological sheltering function S_c. While various sheltering functions have been proposed to describe this attenuation of the fluid flow in the wake of an obstacle (Steele et al. 1989; Lu et al. 2011; Lüpkes et al. 2012), we use here a formulation that is assumed to be valid in both the ocean and the atmosphere:

$$S_c = [1 - \exp(-s_l D/H)]^{1/2}. \tag{9}$$

Following wind experiments on shelterbelts by Nägeli (1946), Hanssen-Bauer and Gjessing (1988) use the attenuation parameter $s_l = 0.18$, while in Lüpkes et al. (2012) the authors compare this formula with results obtained by tunnel observations and modeling (López et al. 2005) and find a better agreement for $s_l = 0.5$. In the reference run of section 4, we use the default value $s_l = 0.18$.

b. Atmospheric and oceanic drag

1) Form drag associated with sail and keels

Arya (1973) was the first author to single out a contribution to the total ANDC on sea ice from pressure ridges. In his original work, in contrast to the derivation in our section 2a, Arya considered the wind velocity at the sail height $U(H_s)$, ignored the sheltering effect described in our section 2a, and integrated the force exerted by the wind on the sails in Eq. (5) over a probability distribution function (PDF) of sail height, where he introduced a minimal cutoff sail height H_{sc} that can contribute to form drag. We find that performing an integration over a realistic PDF of obstacle heights does not significantly modify the drag (Mai et al. 1996), and we will assume in this paper that it is sufficient to use the average value of the parameters of interest to derive the form drag coefficients in the general formulation of Eq. (8). Considering the average sail height H_s and distance between sails D_s, the form drag coefficient resulting from the sails can be written as

$$C_{\mathrm{dar}} = \frac{1}{2} c_{\mathrm{ra}} S_c^2 \frac{H_s}{D_s} A \left[\frac{\ln(H_s/z_{0i})}{\ln(10/z_{0i})}\right]^2, \tag{10}$$

where A is the sea ice concentration, c_{ra} is a local form drag coefficient assumed constant, and z_{0i} is the roughness length of level ice ($z_{0i} = 5 \cdot 10^{-4}$ m in the standard version of CICE; Hunke and Lipscomb 2010). In this expression, assuming a random orientation of sails (Arya 1973; Mai et al. 1996), we have substituted the mean ridging density, or total length of sails per unit area of ice NL/AS_T, by $\mu\pi/2$, where μ is the mean sail frequency defined as the average number of sails per unit length of a linear traverse ($\mu = 1/D_s$, with D_s the distance between sails).

The large part that keels play in the momentum transfer between the ice and the ocean in the Arctic region has long been understood (Pite et al. 1995). In a first approximation, identifying the water to be a homogeneous fluid, this form drag contribution can be expressed in a manner similar to Eq. (10):

$$C_{\mathrm{dwr}} = \frac{1}{2} c_{\mathrm{kw}} S_c^2 \frac{H_k}{D_k} A \left[\frac{\ln(H_k/z_{0i})}{\ln(10/z_{0i})}\right]^2, \tag{11}$$

where we have replaced the obstacle height with the keel depth H_k and the distance between obstacles with the distance between keels D_k. In line with direct numerical simulation of homogeneous fluid flow around discrete obstacles (Le et al. 1997; Leonardi et al. 2003), we assume that the functional dependence of the sheltering function remains the same as in Eq. (9). In reality the homogeneity assumption breaks down in the ocean when the keel depth becomes of the order of the depth of the oceanic boundary layer (Pite et al. 1995; Lu et al. 2011). A detailed parameterization of the momentum transfer resulting from the interaction of a surface topography with flow in a stratified fluid remains beyond the scope of this paper and in what follows we will assume Eq. (11) for all keel depths.

2) Form drag associated with floe edges

Hanssen-Bauer and Gjessing (1988) were the first authors to account for the influence of floe edges on the surface momentum exchange at the ice–atmosphere interface. They introduced a sheltering function similar to Eq. (9), where the distance D is replaced by the typical distance between floes D_f and where the obstacle height H corresponds to the freeboard H_f. If one assumes $A = Nc_{\mathrm{sf}}L^2/S_T$, where L is the average floe length and c_{sf} is a geometrical parameter ($c_{\mathrm{sf}} = \pi/4$ for circular floes and $c_{\mathrm{sf}} = 1$ for square floes), then the total length of the floe edges per unit area can be reformulated to $NL/S_T = A/(c_{\mathrm{sf}}L)$, and the form drag coefficient resulting from the floe edges can be rewritten:

$$C_{\mathrm{daf}} = \frac{1}{2} \frac{c_{\mathrm{fa}}}{c_{\mathrm{sf}}} S_c^2 \frac{H_f}{L} A \left[\frac{\ln(H_f/z_{0w})}{\ln(10/z_{0w})}\right]^2, \tag{12}$$

where c_{fa} is a local form drag coefficient assumed constant, and z_{0w} is the roughness length of water upstream of the floe ($z_{0w} = 3.27 \cdot 10^{-4}$ m; Hunke and Lipscomb 2010). In this expression the quantities L and D_f, contained in the sheltering function S_c, are not provided by current sea ice models and need to be prescribed or parameterized as a function of known variables. Lüpkes et al. (2012) have proposed that the floe length can be expressed as a function of the ice concentration as

$$L = L_{\min}\left(\frac{A_\star}{A_\star - A}\right)^{\beta}, \tag{13}$$

where $A_\star$ is introduced to avoid a singularity at $A = 1$ and $A_\star = 1/[1 - (L_{\min}/L_{\max})^{1/\beta}]$. This parameterization of the floe length is based on the analysis of aircraft data in the Fram Strait in the summer season (Hartmann et al. 1992; Kottmeier et al. 1994) and is therefore expected to break down for the floe length in the winter ice pack. Lüpkes and Birnbaum (2005), assuming periodically distributed square floes, suggest the parameterization of the average distance between floes:

$$D_f = L(1 - \sqrt{A})/\sqrt{A}. \tag{14}$$

Describing the drift of ice floes in the MIZ, Steele et al. (1989) were the first authors to account in a sea ice model for the contribution of floe edges to the oceanic form drag. Here we assume that the form drag associated with floe edges at the ocean–ice interface is similar to the formulation of Eq. (12):

$$C_{\mathrm{dwf}} = \frac{1}{2}\frac{c_{\mathrm{fw}}}{c_{\mathrm{sf}}}S_c^2\frac{D}{L}A\left[\frac{\ln(D/z_{0w})}{\ln(10/z_{0w})}\right]^2, \tag{15}$$

where we have substituted the freeboard H_f for the draft D.

3) Form drag associated with melt pond edges

Lüpkes et al. (2012, 2013), relying on measurements in the summer Arctic (Andreas et al. 2010), suggested that melt ponds could contribute significantly to the total form drag. While it is not yet clear how to accurately treat the combined effect of form drag due to sails and to melt pond edges, we provide here an expression of the form drag coefficient associated with the latter. It is possible that the increase of the melt pond contribution to the total form drag would be associated with a reduction of the contribution from sails. Indeed the formation of ponds can be intuitively understood to fill the asperities formed by sails and therefore reduce the roughness of the ice landscape. It is, on the other hand, possible that the impact of melt ponds is only dominant in smooth ice where sails are rare. If the average area of a pond is $A_{p0} = c_{\mathrm{sp}}L_p^2$, where L_p is the average pond length and c_{sp} is a geometrical constant, then the pond ice area coverage can be written $A_p = Nc_{\mathrm{sp}}L_p^2/(AS_T)$ and Eq. (8) can be reformulated as

$$C_{\mathrm{dap}} = \frac{1}{2}\frac{c_{\mathrm{pa}}}{c_{\mathrm{sp}}}S_c^2\frac{H_p}{L_p}AA_p\left[\frac{\ln(H_p/z_{0w})}{\ln(10/z_{0w})}\right]^2, \tag{16}$$

where c_{pa} is a local form drag coefficient assumed constant and H_p is the typical height difference between the surface of the pond and the surrounding ice. In practice, most ponds reach an equilibrium through drainage and the surface of the pond is at sea level (Eicken et al. 2004; Flocco and Feltham 2007). With this assumption, one can identify $H_p = H_f$. A possible parameterization of the average pond length proposed by Lüpkes et al. (2012) and based on observation of the mean melt pond size by Fetterer and Untersteiner (1998) is

$$L_p = L_{p_{\min}}A_p + L_{p_{\max}}(1 - A_p). \tag{17}$$

4) Skin drag

Arya (1975) is the first author to introduce in the description of the skin drag of level ice a dependence on the sail density. The results are based on observations in wind tunnels (Plate and Lin 1965), later confirmed by direct numerical simulation (Le et al. 1997). The skin drag coefficient is parameterized as

$$C_{\mathrm{das}} = A\left(1 - m_a\frac{H_s}{D_s}\right)c_{\mathrm{sa}}, \quad \text{if} \quad \frac{H_s}{D_s} \geq \frac{1}{m_a}, \tag{18}$$

where m_a is a parameter that depends on the sail height but is often assumed constant ($m_a = 20$ here), and c_{sa} is the unobstructed skin drag that would be attained in the absence of sails and for a complete ice coverage $A = 1$. We choose as a default value $c_{\mathrm{sa}} = 0.0005$. Garbrecht et al. (1999) measured a larger value of $c_{\mathrm{sa}} = 0.0013$, but this value is likely to also include a contribution from the floe edge.

Here again, as in the case of keels and floe edge contribution to oceanic drag, we assume that the shadowing effect parameterized in the atmosphere by Eq. (18) remains of the same functional form in the ocean:

$$C_{\mathrm{dws}} = A\left(1 - m_w\frac{H_k}{D_k}\right)c_{\mathrm{sw}}, \quad \text{if} \quad \frac{H_k}{D_k} \geq \frac{1}{m_w}. \tag{19}$$

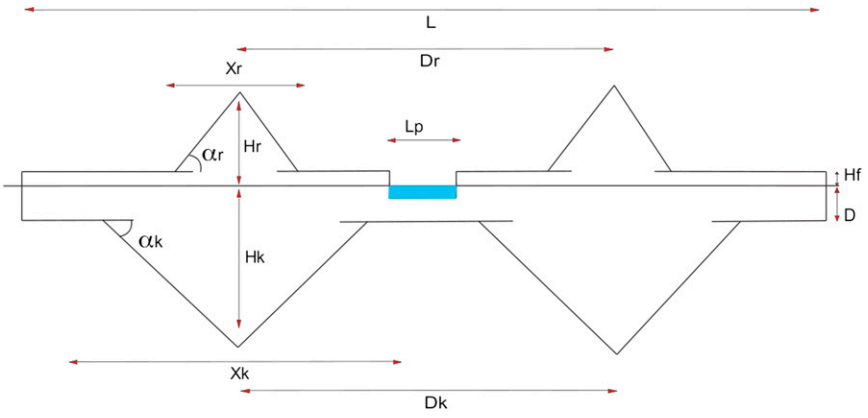

FIG. 1. Schematic representation of an idealized sea ice floe comprising a system of two triangular sails and keels and a single melt pond. The quantities that are needed to derive the ANDC and ONDC are shown: the floes size L, the freeboard H_f [Eq. (26)], the draft D, the pond size L_p, the distance between sails D_s, the distance between keels D_k, the sail and keel heights H_s and H_k, the slopes of the sail and keel α_r and α_k, and the bases of the sail and keel X_s and X_k.

The value $m_w = 10$ is chosen in line with direct numerical simulations of turbulent water flow over model surfaces containing rectangular obstacles (Le et al. 1997; Leonardi et al. 2003). At present c_{sw} is not constrained from observations, therefore we consider this to be a free parameter of the model (default value $c_{sw} = 0.002$).

3. Implementation of the new drag formulation in CICE

a. Diagnosis of sea ice geometry parameters

We incorporate our new drag parameterization into the CICE code (version 4.1), which describes both the thermodynamic and dynamic evolution of the sea ice cover. A description of CICE is contained in the user manual (Hunke and Lipscomb 2010).

1) SAIL (KEEL) HEIGHT AND DISTANCE BETWEEN SAILS (KEELS)

To allow for a realistic representation of thickness-dependent processes, many climate sea ice models, such as CICE, have introduced an ice thickness distribution (ITD), represented in the numerical code by several ice thickness categories. The ridging scheme used in CICE, based on the work of Rothrock (1975), Thorndike et al. (1975), Hibler (1980), and Flato and Hibler (1995), is compatible with a multicategory sea ice model and is described in detail in Lipscomb et al. (2007) and Hunke and Lipscomb (2010). In addition, with the latest version of CICE, version 4.1, one can compute the total volume of level ice v_{lvl} and the total coverage of level ice a_{lvl}. The total volume of ridged ice (accounting also for rafting ice) v_{rdg} and the total coverage of ridged ice a_{rdg} can then be deduced from the total ice volume v_i and the total ice coverage a_i through the requirements that $v_{lvl} + v_{rdg} = v_i$ and $a_{lvl} + a_{rdg} = a_i$.

To relate the small-scale quantities associated with the ridge-building process (ridge height and distance between ridges) to the average grid cell quantities computed in the model, some assumptions are necessary as to the geometry and spatial distribution of the ridges. In Fig. 1, we offer a schematic representation of an ensemble of sails and keels. This oversimplified picture neglects the wide variety of geometries and configurations associated with the ridging processes in the Arctic. For example, as discussed in Martin (2007), there is not always a one to one correspondence between keels and sails; also the triangular shape assumed here for the cross sections of the sails and keels is more representative of a younger, ridged structure in contrast to older sails and keels that have a softer, Gaussian-shaped profile. Using a method described in Haas et al. (2009), Martin (2007) analyzed airborne laser and electromagnetic measurements of the transects of the Arctic sea ice cover and presented a detailed analysis of synchronous measurements of sail and keel height and density as well as of the surrounding thickness of level ice. Based on these observations, Martin offers various possible parameterizations of these quantities.

Notwithstanding these details, here we make the simplifying assumptions that (i) sails and keels have a triangular cross section; (ii) the average keel depth and sail height have a constant ratio $H_k/H_s = R_h$; and (iii) the average distance between keels and distance between sails have a constant ratio $D_k/D_s = R_d$. Following

TABLE 2. Model parameters associated with the reference run FORM.

Ridge parameters	Floe/melt pond parameters	Local drag coefficients	Other parameters
$R_d = 1$	$L_{\min} = 8$ (m)	$c_{ra} = 0.2$	$z_{0w} = 0.000\,326$ (m)
$R_h = 4$	$L_{\max} = 300$ (m)	$c_{kw} = 0.2$	$z_{0i} = 0.0005$ (m)
$\alpha_r = \alpha_k = 22°$	$L_{p_{\min}} = 2.26$ (m)	$c_{fa} = 0.2$	$m_a = 20$
$\phi_s = \phi_k = 0.8$	$L_{p_{\max}} = 24.63$ (m)	$c_{dw} = 0.2$	$m_w = 10$
$\alpha = 0$	$c_{sf} = 0.2$	$c_{pa} = 0.2$	$s_l = 0.18$
$\beta = 0.75$	$c_{sp} = 0.2$	$c_{sa} = 0.0005$	$\rho_i = 917$ (kg m^{-3})
		$c_{sw} = 0.002$	$\rho_s = 300$ (kg m^{-3})

assumption (i) the volume V_s of one sail of height H_s and the volume V_k of one keel of depth H_k are (Steiner et al. 1999)

$$V_s = \frac{1}{2} H_s X_s L_y \quad \text{and} \quad V_k = \frac{1}{2} H_k X_k L_y, \tag{20}$$

where L_y is the transverse extent of the sail and keel, and the sail width X_r and keel width X_k (see Fig. 1) are expressed as

$$X_s = \frac{2H_s}{\tan(\alpha_r)} \quad \text{and} \quad X_k = \frac{2H_k}{\tan(\alpha_k)}, \tag{21}$$

where the sail slope α_r and keel slope α_k are considered free parameters of the model.

To estimate H_s, H_k, D_s, and D_k in CICE, we identify the total volume of the ridged ice in a grid cell of area $S_T = L_x L_y$, $v_{\text{rdg}} S_T$ to be the combined volume of N_s sails and N_k keels that are here assumed for simplicity to extend through an entire cell and be parallel to its side of length L_y (L_x is the length of the other side of the idealized rectangular cell). For a constant spacing between sails and keels, $N_s = a_i L_x / D_s$ and $N_k = a_i L_x / D_k$, using Eq. (20), we can write the total volume of sails and keels as

$$v_{\text{rdg}} = \frac{A}{2} \left(\frac{\phi_s H_s X_s}{D_s} + \frac{\phi_k H_k X_k}{D_k} \right), \tag{22}$$

where we have introduced constant porosities for the sails ϕ_s and keels ϕ_k (default values $\phi_s = \phi_k = 0.8$ as shown in Table 2).

The total area of ridged ice in a grid cell $a_{\text{rdg}} S_T$ can be identified for the total area covered in a grid cell by N_s ridges, $A L_x L_y X_s / D_s$, or by the area covered by N_k keels, $A L_x L_y X_k / D_k$, or even a combination of both. We can then write the area of ridged ice as

$$a_{\text{rdg}} = A \left(\alpha \frac{X_s}{D_s} + \beta \frac{X_k}{D_k} \right), \tag{23}$$

where $0 < \alpha < 1$ and $0 < \beta < 1$ are weight functions. In the following, we will assume that the area of ridged ice can be identified entirely for the area covered by keels and therefore set $\alpha = 0$ (we choose a default value of $\beta = 0.75$; see Table 2).

Combining Eqs. (21)–(23) and eliminating the keel depth and the distance between keels, respectively, through $H_k = R_h H_s$ and $D_k = R_d D_s$, one deduces the following expressions for the sail height,

$$H_s = 2 \frac{v_{\text{rdg}}}{a_{\text{rdg}}} \frac{\alpha \tan\alpha_k R_d + \beta \tan\alpha_r R_h}{\phi_s \tan\alpha_k R_d + \phi_k \tan\alpha_r R_h^2}, \tag{24}$$

and the distance between sails

$$D_s = 2 H_s \frac{a_i}{a_{\text{rdg}}} \left(\frac{\alpha}{\tan\alpha_r} + \frac{\beta}{\tan\alpha_k} \frac{R_h}{R_d} \right). \tag{25}$$

Figures 2b and 2f show the March climatological average over the period 1990–2012 of the estimated average sail height H_s and average distance between sails D_s, ranging from less than 1 m to more than 3 m and from about 40 m to more than 500 m, respectively. Figures 3b and 3f show the same climatologies in September, with values ranging for the sail height from about 1.5 m to more than 3 m and for the distance between sails from about 30 m to more than 500 m. These estimates appear realistic when compared with observations of sail and keel height and frequency over the Arctic Basin as reviewed in Steiner et al. (1999), Mai et al. (1996), and Martin (2007).

2) FREEBOARD, FLOE DRAFT, AND MELT POND EDGE

To calculate the floe edge freeboard H_f and floe draft D in CICE, some approximations are required. First, we assume that the floe edge freeboard and draft are representative of the air–snow and ice–water surface elevation in the bulk of the floe. We do not, for example, consider here the possibility of enhanced elevations at the floe edges due to small pressure ridges at the

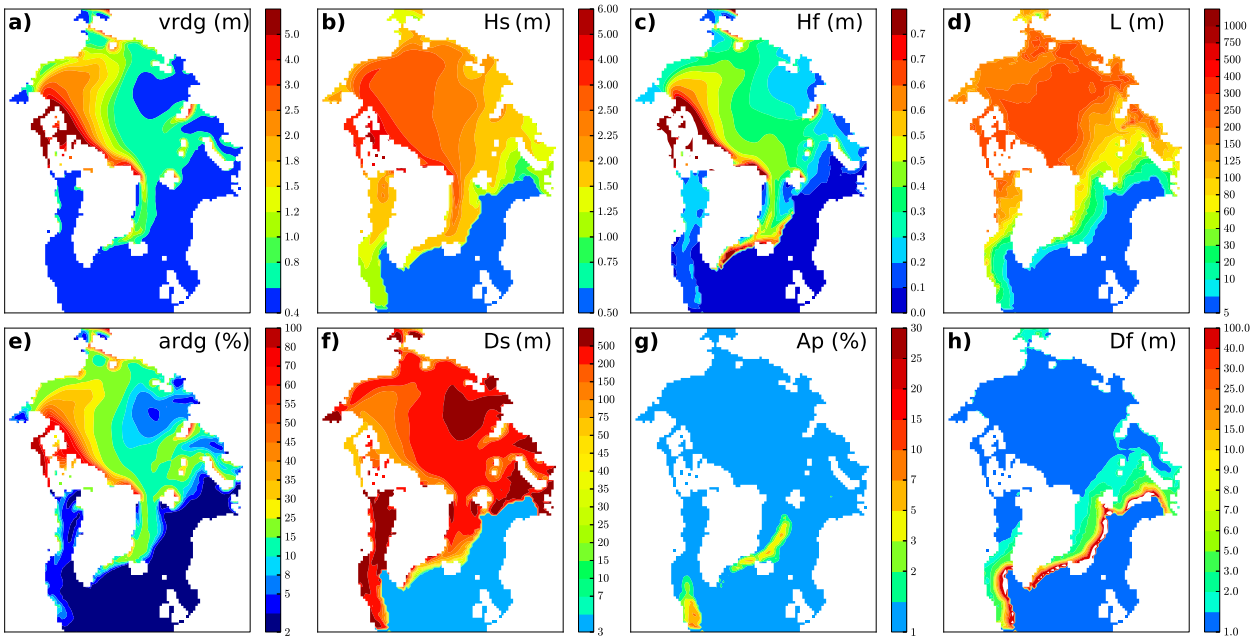

FIG. 2. March climatology (1990–2012) of the intermediate variables introduced in sections 2 and 3. (a) Mean thickness v_{rdg} of ridged ice; (b) sail height H_s as computed in Eq. (24); (c) freeboard H_f from Eq. (26); (d) floe size L from Eq. (13); (e) ice coverage of ridged ice a_{rdg}; (f) distance between sails D_s from Eq. (25); (g) pond area coverage as a fraction of the ice cover A_p; and (h) distance between ice floes D_f from Eq. (14).

upstream and downstream floe edges (Birnbaum and Lüpkes 2002; Kottmeier et al. 1994). With the assumption of hydrostatic equilibrium, the effective ice plus snow freeboard is then given by

$$H_f = H_i(1 - \rho_i/\rho_w) + H_s(1 - \rho_s/\rho_w), \qquad (26)$$

where ρ_i, ρ_w, and ρ_s are, respectively, the densities of sea ice, water, and snow; H_i is the mean ice thickness; and H_s is the mean snow thickness (means are taken over the ice-covered regions). Note that in the above derivation of the floe freeboard and draft, we have ignored the melt pond contribution to hydrostatic equilibrium. In addition,

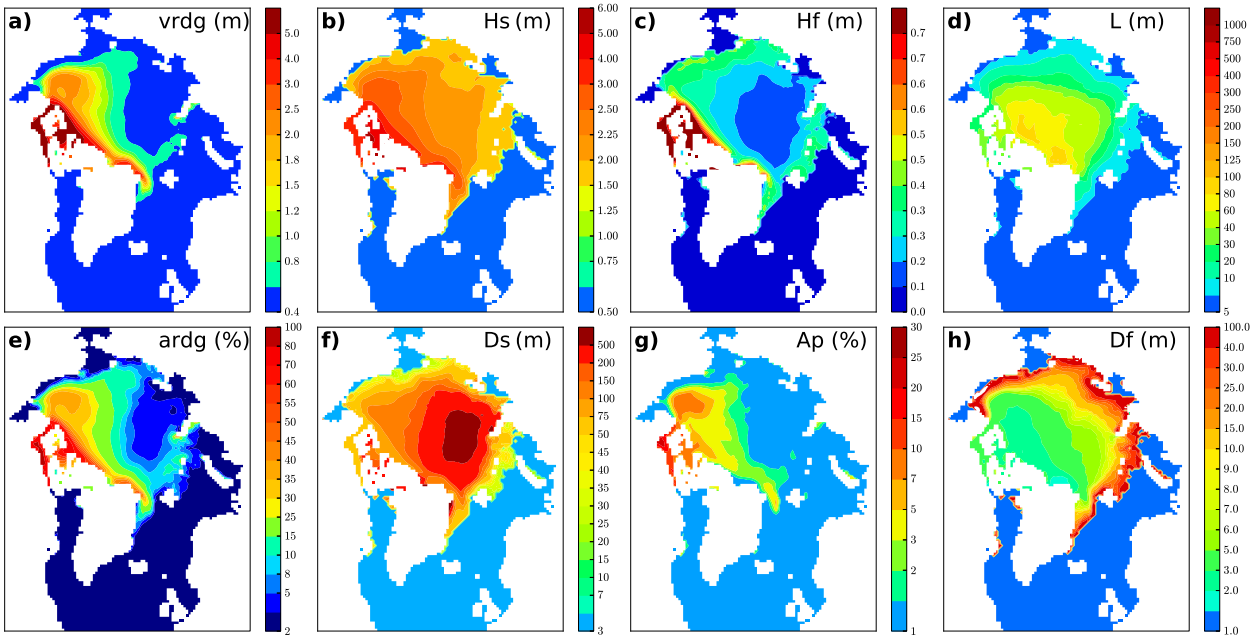

FIG. 3. As in Fig. 2, but for September climatology.

the freeboard and draft are only computed as averages over the entire ice-covered area, and we do not compute these quantities individually for each ice thickness category. The average freeboard over the period 1990–2012 is shown in March and September, respectively, in Figs. 2c and 3c, with values ranging from 10 to 70 cm.

Turning now to the calculation of the melt pond edge elevation H_p, we assume that the Darcy drainage of the melt pond water through the ice occurs at a sufficiently rapid time scale compared to the time scale associated with the evolution of the ice thickness distribution so that the melt pond surface is at the same level as the ocean surface surrounding the floes (Flocco and Feltham 2007; Flocco et al. 2010, 2012). We therefore use the simplified expression of the melt pond edge elevation $H_p = H_f$.

3) FLOE SIZE, DISTANCE BETWEEN FLOES, AND MELT POND SIZE

We have tested the parameterization described in section 1, Eq. (13), for the floe length as a function of sea ice concentration. Figures 2d and 3d show the average floe lengths that result from this approach over the period 1990–2012 in March and September, respectively. In March (September), the average floe size ranges from about 20 m (20 m) in the MIZ to about 400 m (100 m) in the central pack ice. The impact of the choice of the parameterization of the floe length on the drag coefficients will be discussed further in section 5. Again following the parameterization of section 2, we estimate the typical distance between floes with Eq. (14) and illustrate the results in Figs. 2h and 3h, with distances ranging in March (September) from about 50 m (50 m) in the MIZ down to 1 m (2 m) in the pack ice. The estimates of the floe size and distance between floes are compatible with observations in the MIZ (Hartmann et al. 1992; Kottmeier et al. 1994). In the central Arctic, on the other hand, it has been shown (Weiss and Marsan 2004) that the floe size follows a power-law distribution over three orders of magnitude from ~30 m to ~30 km, and hence the average value introduced here is only a crude approximation.

For the average melt pond length L_p, we use the parameterization as a function of melt pond ice coverage A_p, described in Eq. (17) in section 3. Making use of the new melt pond model, now available in the latest release of CICE, that is suitable for forecasting the presence of melt ponds based on sea ice conditions (Flocco and Feltham 2007; Flocco et al. 2010, 2012), we can estimate the average pond area coverage and from the parameterization of Eq. (17) produce an estimate of the average pond size. Figures 2g and 3g illustrate the CICE estimates of the average melt pond concentration respectively in March and September. The pond size is linearly related to the pond concentration and is compatible with observations from declassified high-resolution satellite imagery (Fetterer and Untersteiner 1998).

b. Implementation into CICE

As in the original drag formulation in CICE (Hunke and Lipscomb 2010), the ANDC and ONDC, along with the transfer coefficients for sensible heat C_H and latent heat C_E [Eqs. (2) and (3)], are initialized into a situation corresponding to neutral atmosphere–ice and ocean–ice boundary layers. Here the default CICE constant ANDC, ONDC, and neutral heat transfer coefficients are replaced by coefficients that explicitly account for form drag, C_{da} and C_{dw}, with their various contributions, Eqs. (10), (12), (16), (18), and (11), (15), (19), expressed in section 2b, and

$$C_{da} = C_{dar} + C_{daf} + C_{dap} + C_{das} \quad \text{and}$$
$$C_{dw} = C_{dwr} + C_{dwf} + C_{dws}. \tag{27}$$

The new neutral drag coefficients are calculated in a separate routine and the model remains computationally efficient. Through their dependence on the diagnostic variables described in the previous section, these neutral drag coefficients vary both spatially and temporally. In the same manner as the variables defined in section 3a, we assume that the total neutral drag coefficients are thickness category independent (although we do make use of the ice redistribution through the variables a_{rdg} and v_{rdg}). The main reason is that the different ice thickness categories represented in the model are representative of a sea ice cover where thicker ice alternates with thinner ice over length scales of tens to thousands of meters. This length scale is also comparable to the distance over which the effect of form drag from obstacles affects the fluid flow over the sea ice cover. It is therefore difficult to treat each thickness class independently. This would correspond to the case of floes of a given thickness drifting freely and independently of the other thinner or thicker floes. The reality is that even in the summer season when the sea ice concentration drops often below 90% and the free drift approximation becomes reasonable, the ice floes still contain ridges and do not have a single characteristic thickness. In other words, the ITD over each ice floe is approximately representative of the total ITD.

The total drag coefficients and heat transfer coefficients will also strongly depend on the type of stratification of the atmosphere and the ocean. Here we keep the default configuration of CICE (Hunke and Lipscomb 2010) that accounts for both stable and unstable atmosphere–ice boundary layers (Kauffman and Large 2002). In contrast to the neutral drag coefficients, the stability effect of the

atmospheric boundary layer is calculated separately for each ice thickness category. The stability of the ice–ocean boundary layer is, on the other hand, currently not accounted for.

4. Impact on Arctic sea ice characteristics

a. Reference runs with and without form drag

CICE (version 4.1) is run in stand-alone mode on a 1° tripolar (129 × 104) grid that covers the whole Arctic with a horizontal grid resolution of around 50 km. Atmospheric forcing data are taken from the National Centers for Environmental Prediction–National Center for Atmospheric Research (NCEP–NCAR) reanalysis (Kalnay et al. 1996): 6-hourly 10-m winds, 2-m temperatures, 2-m humidity, daily shortwave and longwave radiation, as well as monthly snowfall and precipitation rates. Sea surface temperature (SST) and salinity are taken from MYO-WP4-PUM-GLOBAL-REANALYSIS-PHYS-001-004 (Ferry et al. 2011) to initialize the Arctic sea ice state. Climatological monthly means from Ferry et al. (2011) are used for the mixed layer salinity (depth of 3 m) and the ocean current (depth of 3 m in most simulations), and a restoration to the SST with a time step of 20 days is applied. In all our runs we use the physically based melt pond model that simulates the evolution of melt ponds based on sea ice conditions described in Flocco et al. (2012). Starting with an isotropic homogeneous sea ice with thickness of 2.5 m, a snow depth of 20 cm, and concentration of 100%, the model is spun up for 10 yr (1980–89) before producing our analysis simulation for 23 yr (1990–2012).

The CICE simulation not accounting for form drag (we denote this reference run SKIN), agrees well with ice concentration data obtained from the Special Sensor Microwave Imager (SSM/I) passive microwave radiometer (PMR) (Figs. 4a–c). The results are also compared with independent datasets of ice thickness and ice motion. For the ice thickness we use the Pan-Arctic Ice Ocean Modeling and Assimilation System (PIOMAS) based on the Parallel Ocean and Ice Model (POIM) of Zhang and Rothrock (2003) (Figs. 4d–f). The sea ice drift data were obtained from the Polar Pathfinder Daily 25-km EASE-Grid Sea Ice Motion Vectors dataset developed by Fowler (2003) (Figs. 4g–i). In line with the default settings of version 4.1 of CICE that was chosen in this work, we used the strength parameterization of Rothrock (1975) and Lipscomb et al. (2007) and set the empirical parameter that accounts for frictional energy dissipation to be $C_f = 10$. To calculate the stress between the ocean and ice, we set the turning angle to zero, used an ANDC of $C_{\mathrm{da}}^{\mathrm{SKIN}} = 0.0013$ (roughness length of $z_a = 0.16$ mm), and an ONDC of $C_{\mathrm{dw}}^{\mathrm{SKIN}} = 0.0061$ ($z_w = 6$ cm). For the rheology we used an elliptical yield curve with a standard value of the ratio of the major to minor axes of the elliptical yield curve, where $e = 2$. All remaining parameters of the model were set to the standard values used in version 4.1 of CICE (Hunke and Lipscomb 2010).

In the following section, we compare the CICE simulation using the new drag formulation of Eq. (27) (we call this new reference run FORM) to that obtained using the version of the code that does not account for form drag. Because our aim is to show the impact of the new parameterization against what can be achieved with a suitable calibration of the uniform drag coefficients we chose, in the reference FORM run, a set of parameters (see Table 2) that guarantees temporally and spatially averaged ANDC and ONDC equal to the neutral drag coefficients in the reference SKIN simulation while maintaining realistic values of the ridged ice height and frequency. Note that keeping the average ANDC and ONDC equal in the FORM and SKIN runs will reduce the apparent impact of the FORM drag. The procedure by which we have obtained the reference FORM run is described in the supplemental material at the Journals Online website (http://dx.doi.org/10.1175/JPO-D-13-0215s1.pdf and http://dx.doi.org/10.1175/JPO-D-13-0215s2.tex) of this paper. All other parameters in the reference FORM run are kept identical to the SKIN reference run. We denote the spatial average of a quantity X as $\langle X \rangle$ and the temporal average as $\overline{X}$. Because of the large number of free parameters of the model (see section 2 and Table 2), one can produce a multiplicity of reference runs accounting for form drag satisfying the criteria $\langle \overline{C}_{\mathrm{da}} \rangle = C_{\mathrm{da}}^{\mathrm{SKIN}}$ and $\langle \overline{C}_{\mathrm{dw}} \rangle = C_{\mathrm{dw}}^{\mathrm{SKIN}}$. Nevertheless, the reference FORM run described in the following section corresponds to a realistic choice of parameters and is constrained by observations. In addition, in the sensitivity study of section 5 we demonstrate the impact of varying the main parameters of the new drag formulation.

In the following sections we first compare the simulation results using the reference FORM and SKIN models and then discuss our sensitivity tests with regard to the free parameters of the FORM model, introduced in section 2.

b. Relative importance of the various contributions to the total drag

1) Arctic central pack–ridge-dominated drag

Figures 5a and 6a (Figs. 5f and 6f) show the climatological total ANDC (ONDC) C_{da} (C_{dw}), respectively in March and August, that corresponds to the maximum

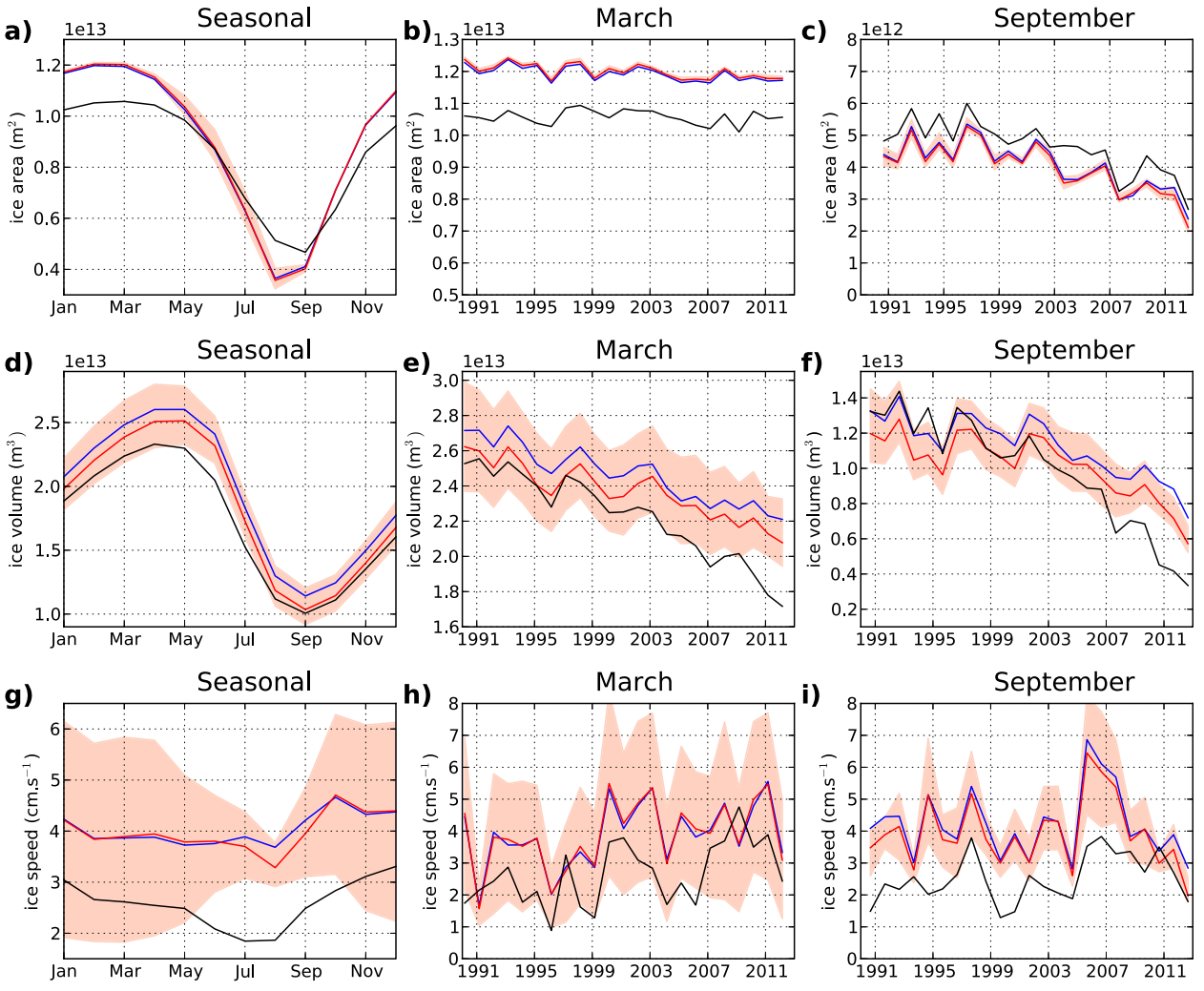

FIG. 4. Seasonal climatology over the period 1990–2012 of the (a) total ice area, (d) total ice volume, and (g) averaged ice speed. The 1990–2012 Arctic March (b) total ice area, (e) total ice volume, and (h) averaged ice speed and September (c) total ice area, (f) total ice volume, and (i) averaged ice speed. The blue lines correspond to the reference SKIN run, the red lines correspond to the reference FORM run, and the black lines correspond to observations. The red shaded areas correspond to the range of values obtained in the sensitivity study summarized in Table 3. In these plots, the black line corresponds respectively to the total ice area obtained from HadISST data in (a)–(c), to the total ice volume from PIOMAS in (d)–(f), and to the average ice speed from Pathfinder in (g)–(i). In (a) to (f), the total quantities are integrated over areas where HadISST data are available. In (g) and (i), the average is computed over a central region of the Arctic Basin, 150 km from the coasts.

sea ice extent and maximum average value for the drag coefficients. The figures show a wide range of values for the ANDC (ONDC) ranging from between 3×10^{-4} and 9×10^{-3} (2×10^{-3} and 4×10^{-3}) in the east over different types of sea ice in the Arctic Ocean, in the Baffin Bay, and Davis Strait to values larger than $\sim 3 \times 10^{-3}$ (10^{-2}) along the west coast of the Arctic Ocean and in the Canadian Archipelago. These values are coherent with measurements of ANDC (Guest and Davidson 1991; Schröder et al. 2003) and ONDC (Lu et al. 2011; McPhee 2012) in the Arctic.

With our new implementation in CICE, each contribution to the total neutral drag coefficients can be isolated [see Eq. (27)]. Comparing Figs. 5a and 5b it is clear that in March the total ANDC is dominated by the contribution from the form drag associated with sails. This is particularly true in the Canadian Archipelago and north of Greenland, where sea ice is subjected to large compressive stresses and the total volume and area of ridged ice are high, as shown in Figs. 2a and 2e, and the typical sail height and sail frequency can reach values as high as 3 m and 20 km^{-1}, respectively, Figs. 2b and 2f. The typical keel height and frequency are related to the sail height and frequency by two constants of proportionality and are therefore not shown. These ridge-dominated form drag areas extend in March over

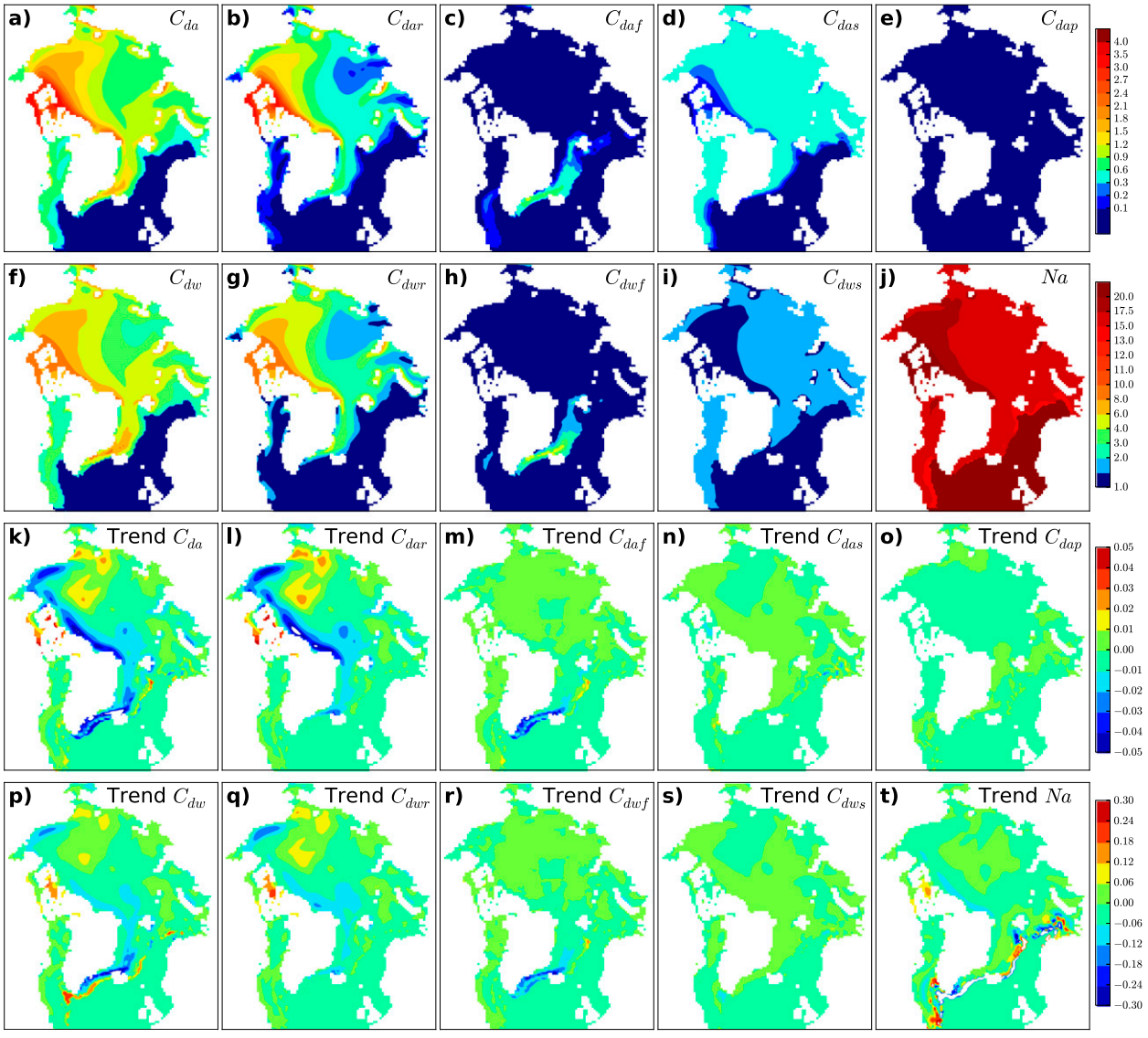

FIG. 5. March climatological (1990–2012) (a) ANDC and its main contributions from (b) sails, (c) ice floe edge freeboard, (d) skin drag, and (e) melt pond edge, and (f) ONDC and its main contributions from (g) keels, (h) ice floe edge draft, and (i) skin drag. (j) The Nansen number $\mathrm{Na} = \sqrt{\rho_a C_{\mathrm{da}}/\rho_w C_{\mathrm{da}}}$. (k)–(t) The corresponding trends computed over the period 1990–2012 (yr^{-1}). Note that all quantities are multiplied by a factor of 10^3.

most of the western part of the Arctic Ocean, with the highest density of sails in the Canadian Archipelago and off the coasts of Greenland, Canada, and Alaska. Excluding the contribution from the regions with lower ice concentration that are localized in March in the ice edge, we see from Figs. 5a, 5b, and 5d that the skin drag C_{das} constitutes most of the remaining contribution to the total ANDC. For most regions, the contribution from the skin drag is equal to the unobstructed skin drag ($c_{\mathrm{sa}} = 0.0005$). This is coherent with Eq. (18), which predicts that the skin drag should only vanish when the product of the average sail height H_s by the average sail frequency $1/D_s$ exceeds $1/m$, with $m = 20$ for the atmospheric skin drag. This condition is satisfied in March only in regions with a sufficiently high density of large sails, where $H_s \geq 2.5\,\mathrm{m}$ (Fig. 2b) and $1/D_s \geq 20\,\mathrm{km}^{-1}$ (Fig. 2f), mainly in the Canadian Archipelago, and breaks down in most of the remaining Arctic Basin, essentially due to a sharp drop of the sail frequency in the model. As can be deduced from Fig. 7a, the combined average contribution to the ANDC from sails (green columns) and from skin drag (yellow columns) varies seasonally. The maximum of C_{dar} (minimum in C_{das}) in the summer season (June, July, and August) comes from the fact that this average

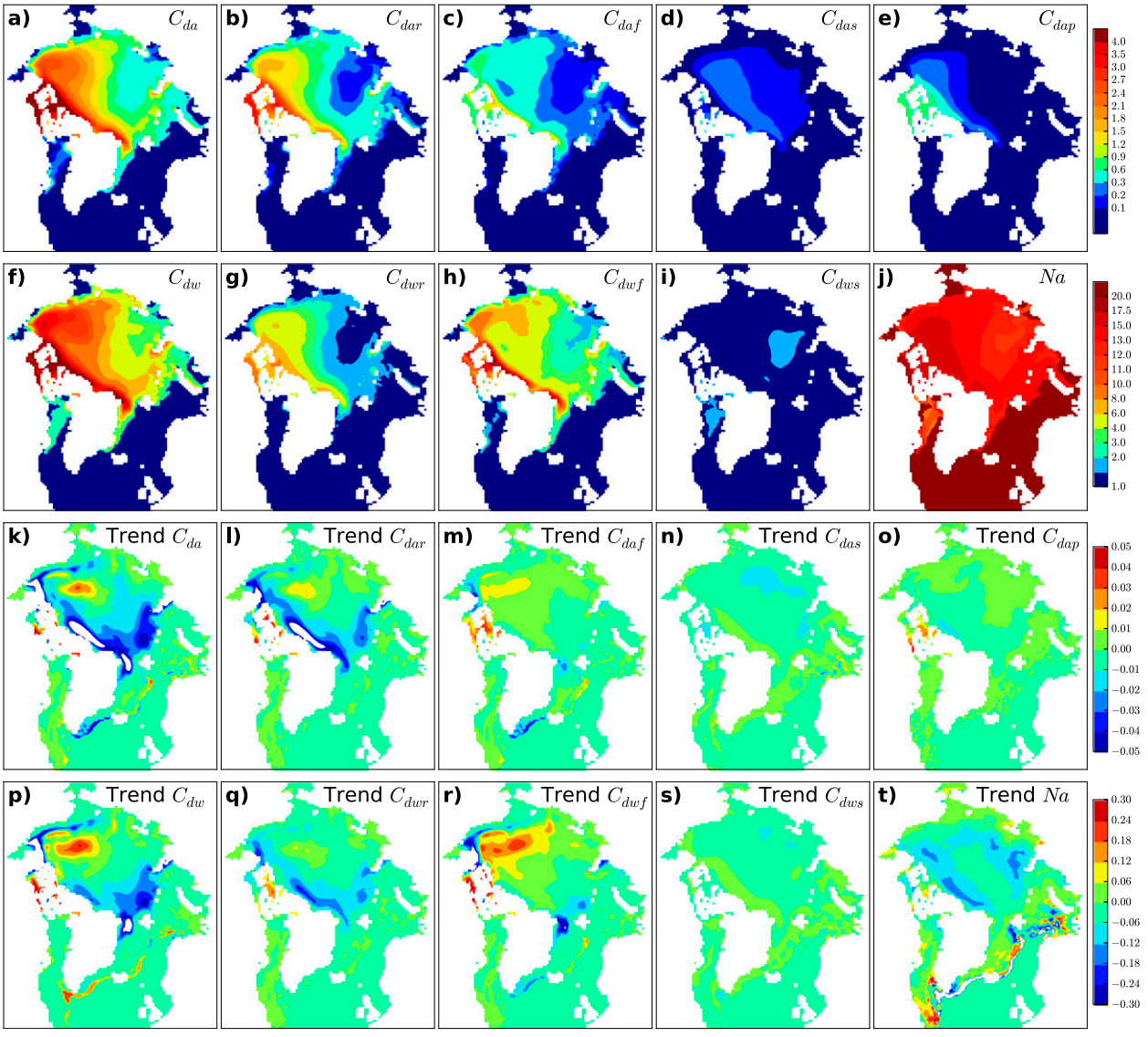

FIG. 6. As in Fig. 5, but for August climatology (1990–2012).

drag coefficient is then computed over essentially multiyear ice that contains on average more ridged ice, while a maximum of C_{das} (minimum in C_{dar}) in autumn (October, November, and December) is associated with the newly formed ice that has had no time to form ridges (not shown).

The discussion above concerning the partition of the ANDC can be duplicated almost exactly for the ONDC that is also dominated in March by the combined contributions of the form drag associated with the keels and to the smaller oceanic skin drag. Figure 7 shows that outside the summer season the three main contributions to the total neutral drag coefficients remain roughly in the same proportion that reflects the similarity in the spatial distribution of these coefficients in both the atmospheric (Figs. 5a–d) and in the oceanic cases (Figs. 5e–h).

2) SUMMER ARCTIC SEA ICE AND MIZ–FLOE EDGE-DOMINATED DRAG

In the winter, the concentration of open water in the central pack ice (far from the ice edge) is very low (less than 2%; see Fig. 8a), therefore reducing the contribution of floe edges to the form drag, with a dominant contribution from sails and keels. As the sea ice concentration diminishes through the summer season, due to melting, to reach a minimum in late September (with concentrations in the central pack of less than 90%; see Fig. 9a), the intermediate quantities, introduced in

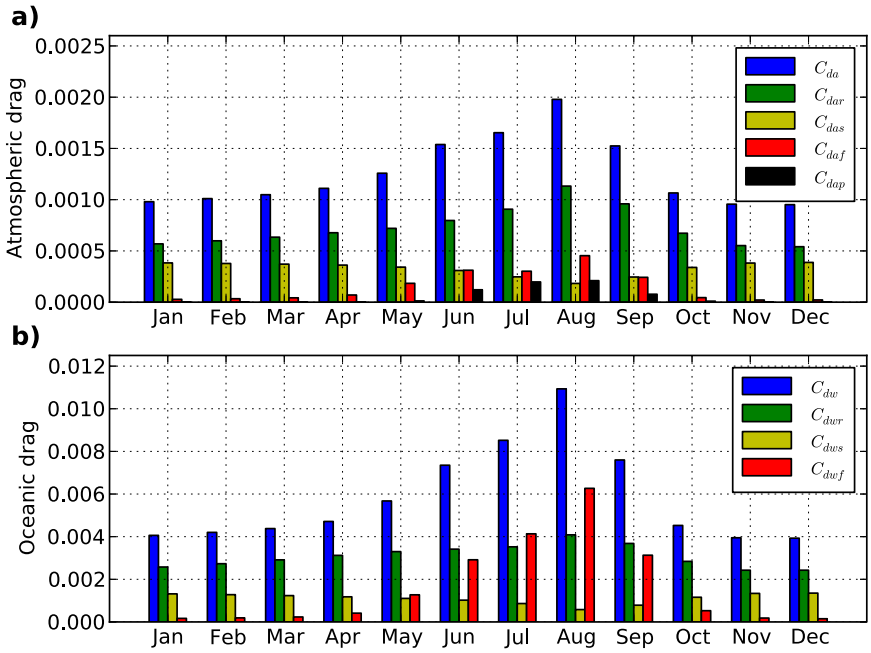

FIG. 7. Climatological (1990–2012) total (a) ANDC and (b) OCND (blue) averaged over the entire Arctic Basin where ice concentration is larger than 15% for every month of the year and the main contributions from floe edges (red), ridges (green), skin drag (yellow), and melt pond edges (black).

section 3a, evolve in the model Arctic configuration. Through the summer months, the sails and keels lose up to a third of their height through melting (see spatial distribution on the maps of Figs. 2b and 3b). The total freeboard accounting for the accumulated snow layer shrinks from an average of $\langle H_f \rangle = 0.3$ m in March to a minimum in September of $\langle H_f \rangle = 0.24$ m (Figs. 2c, 3c). The evolution of the floe length and the distance between floes is related to the ice concentration through the parameterization introduced by Lüpkes et al. (2012) and reproduced in Eqs. (13) and (14). As the ice concentration reaches a minimum in August so does the average floe length with a minimum value of $\langle L \rangle \sim 10$ m, from its winter maximum in March of $\langle L \rangle = 120$ m, while the average distance between floes increases from its winter average minimum $\langle D_f \rangle \sim 2$ m to its August maximum $\langle D_f \rangle \sim 10$ m (see maps in Figs. 2d,h and 3d,h). Note that for simplicity we keep in this paper the original formulation of lateral melting used in CICE that assumes a constant effective floe diameter of 300 m, and therefore the parameterization of the floe length $L(A)$ does not influence directly the evolution of the ice concentration.

As can be seen from Figs. 7a and 7b, the spatially averaged form drag associated with floe edges, both for the atmosphere $\langle C_{\mathrm{daf}} \rangle$ and the ocean $\langle C_{\mathrm{dwf}} \rangle$, increases dramatically in the summer months (starting in May and culminating in August) and even becomes the dominant contribution to the total drag coefficient in the oceanic case. The maps showing respectively C_{daf} and C_{dwf} in March (Figs. 5c and 5h) and in September (Figs. 6c and 6h) illustrate the fact that while the increase of form drag associated with floe edges is maximal in the MIZ, it is also important in the pack ice. Turning to Eqs. (12) and (15), we see that this increase results essentially from the competing effect of a reduction of the typical floe length that tends to increase C_{daf} (C_{dwf}) and a freeboard (draft) height reduction in the summer that tends to reduce C_{daf} (C_{dwf}). As the floe length is reduced more dramatically than the freeboard (or draft), it is the former effect that will dominate, and the drag coefficients C_{daf} and C_{dwf} will be larger in the summer. This shows that the parameterization of the floe length plays a crucial role in the correct estimate of the form drag coefficient, particularly in the summer.

The symmetry between the atmospheric and oceanic drag coefficients, described in the previous section 1, breaks down in the summer due to the larger increase of the floe edge contribution in the ocean (cf. Figs. 5c and 5h) and can be understood by comparing the ratios $C_{\mathrm{dwr}}/C_{\mathrm{dar}} \simeq 3$ and $C_{\mathrm{dwf}}/C_{\mathrm{daf}} \simeq 10$, where the difference is mainly due to the large ratio of the floe draft over the floe freeboard d/h_f. Hence, while in the winter the contribution from the floe edges is confined to the MIZ and

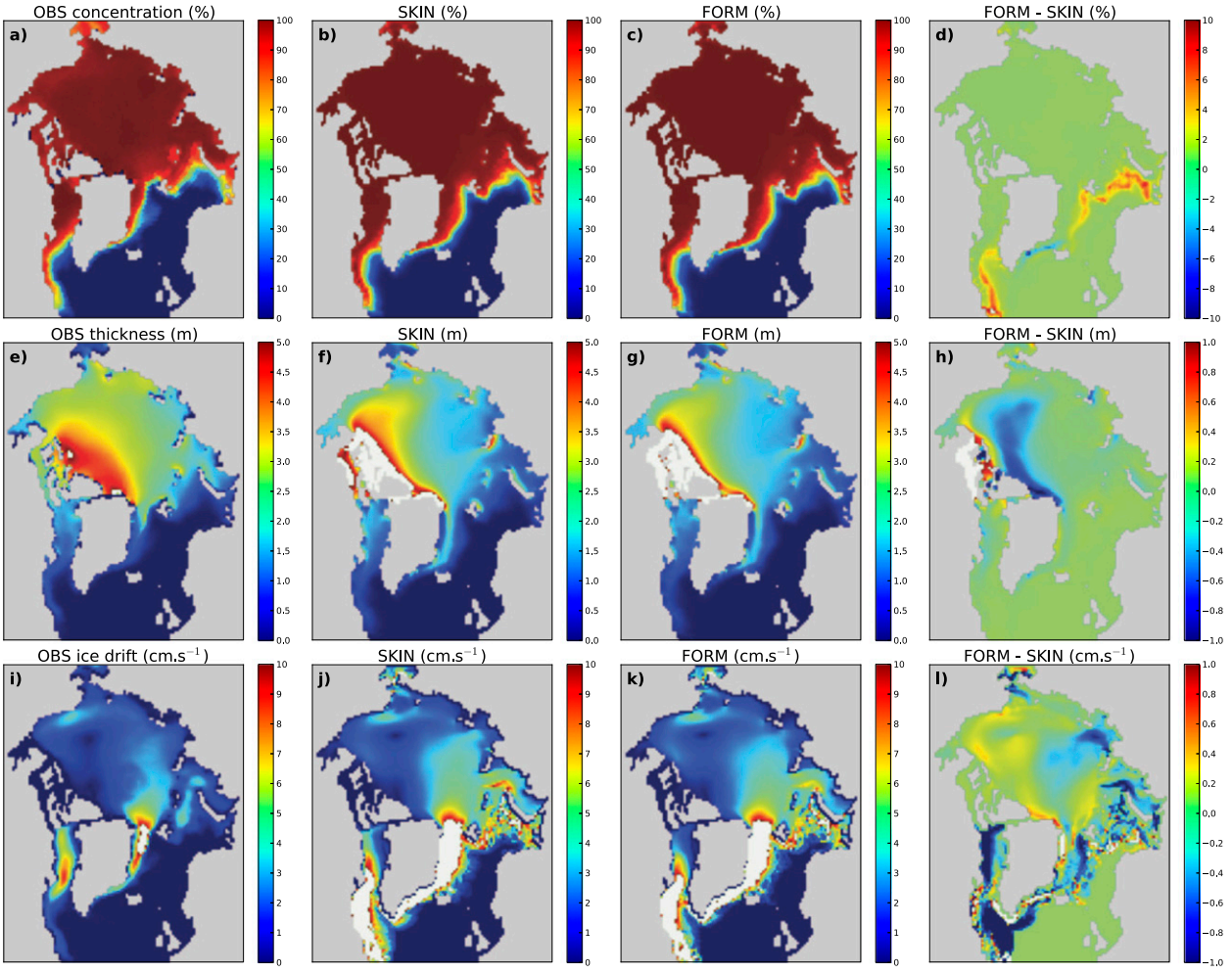

FIG. 8. Climatological (1990–2012) March ice concentration from (a) HadISST measurements, (b) the SKIN run, (c) the FORM run, and (d) ice concentration difference between the FORM and SKIN runs. Same climatologies for ice thickness from (e) PIOMAS, (f) the SKIN run, (g) the FORM run, and (h) ice thickness difference between the FORM and SKIN runs. Also shown climatologies for the ice drift from (i) Pathfinder, the (j) SKIN run, the (k) FORM run, and (l) ice drift difference between the FORM and SKIN runs. Note that regions where the values exceed the range in the color bar are shown in white.

is therefore small, in the summer it contributes substantially to the total drag coefficients and even becomes the main contribution in some regions in the oceanic case.

3) MELT SEASON–MELT POND CONTRIBUTION

Melt ponds are only present during the melt season (mainly from June to August) and cover regionally up to ≃60% of the sea ice in July [see Fig. 4 of Flocco et al. (2012)]. Their relative contribution to the total ANDC is then ≃10% (Fig. 7a) and becomes of a similar magnitude as the contributions from skin drag and floe edges. Here we have assumed that the presence of melt ponds acts only as a source of additional drag, but in reality it is also possible that the formation of melt ponds is accompanied by a reduction of the skin drag contribution due to a smoothing effect of the ponds over the ice (the ponds fill the small asperities in the sea ice). In the absence of such a smoothing effect, the impact of the ponds is of leading order, and, in line with Andreas et al. (2010), we attribute most of the increase of the total ANDC in the summer to the combined contributions of melt pond and floe edges. One must also note that in our parameterization melt ponds do not contribute to the ONDC and are therefore inducing an increase in the ratio C_{da}/C_{dw}.

A quantity that quantifies the importance of the ratio C_{da}/C_{dw} on the ice dynamics is the Nansen number defined as $\mathrm{Na} = \sqrt{\rho_a C_{da}/\rho_w C_{dw}}$. This quantity has long been used as an estimate of the ice speed as a fraction of the wind speed and becomes exact when the internal forces in the ice can be neglected, the ocean is stagnant,

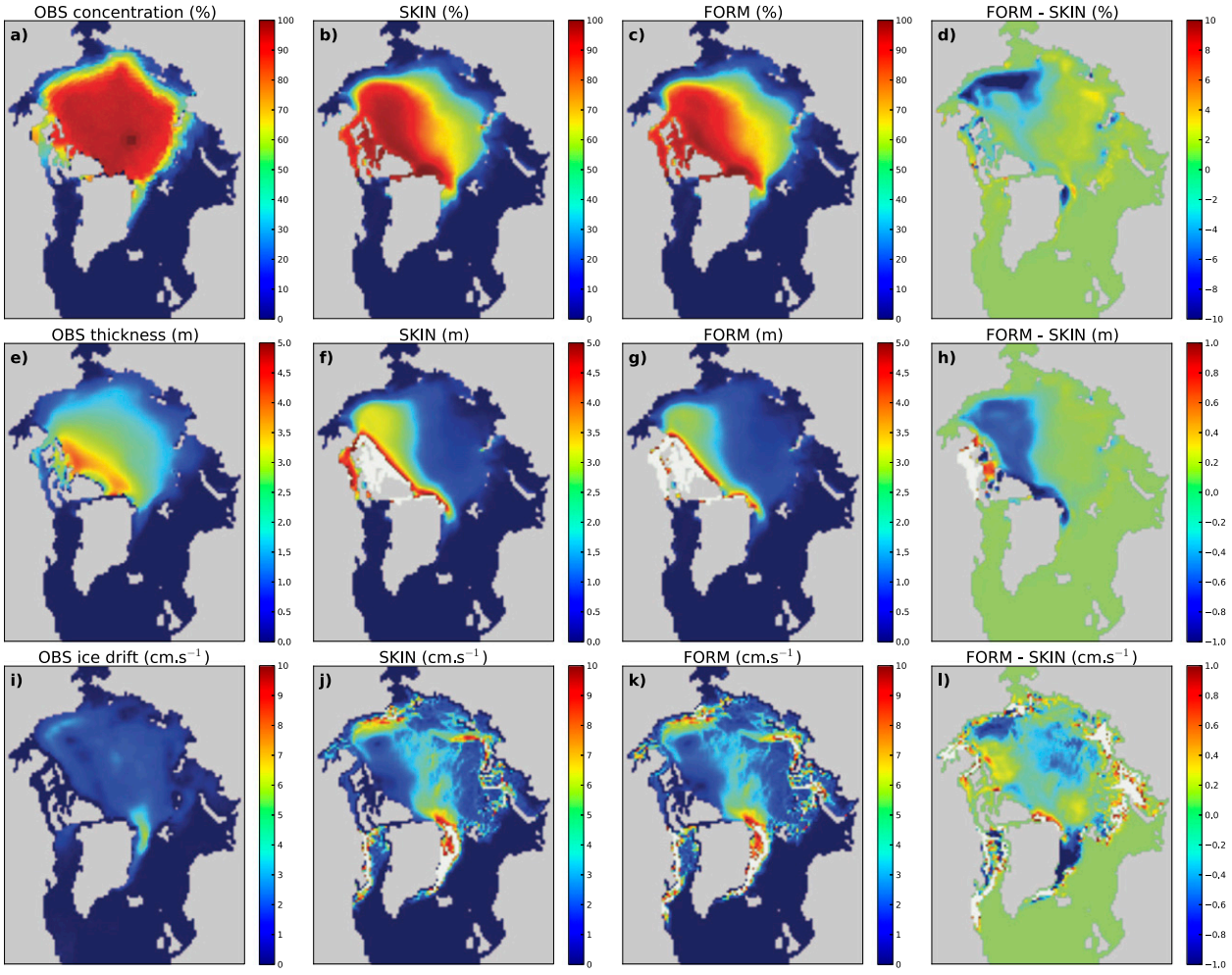

FIG. 9. Climatological (1990–2012) September ice concentration from (a) HadISST measurements, (b) the SKIN run, (c) the FORM run, and (d) ice concentration difference between the FORM and SKIN runs. Same climatologies for ice thickness from (e) PIOMAS, (f) the SKIN run, (g) the FORM run, and (h) ice thickness difference between the FORM and SKIN runs. Also shown climatologies for the ice drift from (i) Pathfinder, (j) the SKIN run, (k) the FORM run, and (l) ice drift difference between the FORM and SKIN runs. Note that regions where the values exceed the range in the color bar are shown in white.

and the only forces acting are the air drag and ocean drag. Typical values found in the Arctic Ocean are Na = 1.7% at a geostrophic reference and Na = 2.5% at a surface reference (Leppäranta 2005). In the reference SKIN run, the Nansen number takes the single value Na = 1.65%. Figures 5j and 6j show the Nansen number (multiplied by a factor of 10^3) in the FORM reference run respectively in March (1.3% < Na < 2.0%) and August (1.2% < Na < 2.0%) with the lowest values realized at the ice edge. The observed decrease near the ice edge reflects the reduced ice drift in these regions within the new parameterization (see Figs. 8l, 9l). Throughout the year large values of the Nansen number can be found in heavily ridged regions in the Canadian Archipelago and north of Greenland (Na = ~1.8%). There the direct correlation between the Nansen ratio and the ice drift is reduced because of the larger internal sea ice stresses.

To summarize, we have demonstrated that the new drag parameterization results in a wide temporal and spatial variability of the ANDC and ONDC over the Arctic Basin. Spatially, the range of values goes from $C_{da} < 5 \times 10^{-4}$ and $C_{dw} < 3 \times 10^{-3}$ along most of the eastern part of the Arctic Ocean and in the Baffin and Davis Strait to $C_{da} \geq 3 \times 10^{-3}$ and $C_{dw} \geq 15 \times 10^{-3}$ in the Canadian Archipelago and north of Greenland. Temporally, the basin-averaged drag coefficients evolve from a minimum in December with $\langle C_{da} \rangle = \sim 1.0 \times 10^{-3}$ and $\langle C_{dw} \rangle = \sim 4 \times 10^{-3}$ to a maximum in August of $\langle C_{da} \rangle = \sim 2.0 \times 10^{-3}$ and $\langle C_{dw} \rangle = \sim 1.1 \times 10^{-2}$. These

TABLE 3. Arctic Basin scale and temporal average over the period 1990–2012 of the ANDC, ONDC, ridge height, distance between ridges, floe size, sea ice volume, sea ice extent, and sea ice drift. In addition to the two reference SKIN and FORM runs, we have performed a sensitivity study of the model and have tested different values of local drag coefficients. The percent is expressed relatively to the reference SKIN run values.

Parameters	$\langle \overline{C}_{da} \rangle \times 10^3$	$\langle \overline{C}_{dw} \rangle \times 10^3$	$\langle \overline{H}_r \rangle$ (m)	$\langle \overline{D}_r \rangle$ (m)	$\langle \overline{L} \rangle$ (m)	$\langle \overline{\text{Ice volume}} \rangle \times 10^{12}$ (m^3)	$\langle \overline{\text{Ice extent}} \rangle \times 10^{12}$ (m^2)	$\langle \overline{\text{Ice speed}} \rangle$ ($cm\,s^{-1}$)
Reference SKIN run	1.31	6.09	—	—	—	19.25	10.19	4.05
Reference FORM run	1.31	6.09	2.27	420	100	18.27	10.27	3.95
$c_{ra} = 0.1$, $c_{rw} = 0.1$	0.89	4.32	2.33	441	103	98.4%	100.7%	94.9%
$c_{ra} = 0.1$, $c_{rw} = 0.3$	0.85	6.93	2.42	478	108	97.4%	100.6%	78.0%
$c_{ra} = 0.3$, $c_{rw} = 0.1$	1.75	7.89	2.24	407	99	101.2%	99.4%	103.1%
$c_{ra} = 0.3$, $c_{rw} = 0.3$	1.95	5.12	2.18	374	91	106.2%	99.5%	132.3%
$c_{fa} = 0.1$, $c_{fw} = 0.1$	1.25	5.31	2.28	411	100	101.9%	100.6%	101.6%
$c_{fa} = 0.1$, $c_{fw} = 0.3$	1.25	7.04	2.28	417	100	102.2%	100.4%	96.6%
$c_{fa} = 0.3$, $c_{fw} = 0.1$	1.37	5.18	2.26	422	100	98.2%	99.7%	104.7%
$c_{fa} = 0.3$, $c_{fw} = 0.3$	1.37	6.85	2.26	426	101	98.6%	99.5%	98.9%
$c_{sa} = 10^{-4}$, $c_{sw} = 4 \times 10^{-4}$	0.78	4.02	2.43	871	106	92.3%	101.2%	82.1%
$c_{sa} = 10^{-4}$, $c_{sw} = 4 \times 10^{-3}$	0.70	6.29	2.52	1170	112	92.0%	101.1%	61.1%
$c_{sa} = 10^{-3}$, $c_{sw} = 4 \times 10^{-4}$	1.88	6.50	2.16	233	94	112.1%	100.4%	133.1%
$c_{sa} = 10^{-3}$, $c_{sw} = 4 \times 10^{-3}$	1.76	7.61	2.22	330	97	104.8%	99.6%	108.2%
$c_{pa} = 0.1$	1.29	6.12	2.27	419	100	100.7%	100.1%	99.7%
$c_{pa} = 0.3$	1.33	6.06	2.26	421	100	99.3%	99.9%	100.3%

values are consistent with the range of values that have been measured experimentally both for the ANDC (Guest and Davidson 1991; Schröder et al. 2003; Andreas et al. 2010) and the ONDC (Lu et al. 2011; McPhee 2012).

c. *Impact on Arctic sea ice state*

1) ARCTIC SEA ICE EXTENT AND AREA

The seasonal climatology (Fig. 4a) as well as the evolution of the March (Fig. 4b) and September (Fig. 4c) ice area over the period 1990–2012 show that the new drag formulation (FORM run), in comparison to the reference run with constant drag coefficients (SKIN run), introduces a minor change to the total area covered by sea ice both in March and September. Both reference runs reproduce well the temporal variability and trend of the observed total ice extent. In March, both models overestimate the total area by around 10% that we attribute mainly to the SST restoring the time scale of 20 days that allows too much ice to form in the Fram Strait (see Figs. 8b,c). In September, both simulations capture well the decreasing trend observed in the Hadley Centre Sea Ice and Sea Surface Temperature (HadISST) dataset. The FORM run total area is on average $\sim 10^{11}\,m^2$ (Table 3) smaller than the SKIN run. The winter ice extent for both simulation runs is mainly constrained in our stand-alone simulation by the strong, warm ocean heat fluxes at the Bering and Fram Straits. Looking at the characteristic spatial features on the maps of Figs. 9b and 9c, we see that the summer ice extent, on the other hand, shows differences with an overall decrease of the ice concentration over the ice edge in the new FORM reference run, with the decrease most acute along the western Arctic ice edge, with the ice not penetrating as deeply in the Fram Strait and in the Canadian Archipelago and being particularly depleted in the Beaufort Sea. We see that regions of lower concentration are associated with regions of thinner ice. The new form drag formulation introduces an additional contribution to the temporal variability in the state of the September Arctic sea ice extent (Figs. 4c).

2) ARCTIC SEA ICE THICKNESS

The seasonal cycle of Fig. 4d and the temporal evolution of Figs. 4e and 4f, as well as Table 3, show that the reference run FORM produces a total Arctic volume of ice reduced on average throughout the year by about $\simeq 1 \times 10^{12}\,m^3$ in comparison with the reference run SKIN. This corresponds in September to a relative total volume of ice decrease of up to 15% (September 2012). The new drag formulation captures well the variability of the total ice volume as estimated by the PIOMAS model (Figs. 4e,f), but underestimates the decrease of the total volume both in March and September (−55% in September from 1990 to 2012 for the FORM run against −75% for PIOMAS). As shown in Figs. 8e–h, the reduced volume of ice in the FORM run is associated with a thinner spatial distribution of ice over a large portion of the Arctic Basin with an acute reduction of sea ice thickness (∼1 m) along the west coast of the Arctic Ocean, north of Greenland, and in the Beaufort Sea. The ice thickness over most of the east portion of the Arctic Ocean is, on the other hand, only slightly reduced

and a noticeable increase of ice thickness is visible in the Canadian Archipelago. To explain this difference in the ice thickness pattern between the FORM and SKIN reference simulations one needs to compare the modification in the contribution to ice thickness from ice transport, thermodynamics, and ridging. Seasonal climatologies of these three contributions (not shown) reveal that thermodynamics is the dominant factor. The regions where ice is mostly depleted correspond to the heavily ridged regions where the drag coefficients and heat transfer coefficients are at maximum (see Figs. 5 and 6) and are therefore the location of increased heat fluxes. Looking at the seasonal evolution of the thermodynamic ice growth in these regions, it appears that the resulting increased ice growth in the winter is more than compensated by a larger melting in the summer. These characteristics are in qualitative agreement with the Cryosphere Satellite (CryoSat) data that show that current models tend to underestimate ice thickness near the North Pole and overestimate ice thickness in the Beaufort Sea (Laxon et al. 2013).

d. *Impact on Arctic sea ice dynamics*

1) ARCTIC SEA ICE DRIFT

In Figs. 8i–l and 9i–l, the climatological averages of the sea ice speed amplitude are shown for the FORM and SKIN runs as well as for the Pathfinder dataset in March and September. While both models capture well the spatial patterns of the ice drift, they tend to overestimate its magnitude [our model results can be compared to other model results and observations (Martin and Gerdes 2007)]. Comparing the Pathfinder dataset with drifting buoys data provided by the International Arctic Buoy Programme (IABP) shows that the former underestimates the monthly averaged drift. We therefore do not attempt a quantitative optimization of our model against this dataset. In September, the average difference between FORM and SKIN follows a complex pattern with alternating neighboring regions of increased and decreased ice speed and strong year-on-year variability (not shown). The pattern is clearer in March, where marked ice speed decreases are noticeable on average in the FORM run in the Baffin Bay, Laptev Sea, and in the Fram Strait, while a slight increase of the ice speeds can be seen over most of the west portion of the Arctic Ocean, reflecting the sea ice thickness decrease in that region. Nevertheless, looking at individual years (not shown) we note that these spatial features are fluctuating and can even be reversed in different years. We attribute at least some of this variability to the condition of stability of the atmospheric boundary layer and its resulting impact on the total atmospheric drag coefficient.

The time evolution of the average ice drift over the whole Arctic is shown in March and September in Figs. 4g–f for the reference FORM and SKIN models and compared with the averaged ice drift obtained from the Pathfinder dataset. The averages are here computed over a central portion of the Arctic Basin 150 km from the coast and therefore excluding the regions of very high ice drift (almost an order of magnitude larger) around the Fram Strait, Greenland Sea, Baffin Bay, and Davis Strait that would otherwise dominate the average ice drift values. Comparing Figs. 4h and 4i, we see that the impact of the new drag laws is on average weak both in March and September. Overall, both the SKIN and FORM runs capture well the temporal variability but overestimate the observed average ice drift values by up to 50%. Note that setting the ocean currents to zero reduces the average drift in the models (not shown). No clear trend is visible in September in both models and observation, but the March model results show an increase over the integration period from an average of about 3 to about 4 $\mathrm{cm\,s^{-1}}$. The increase in the model captures qualitatively the increase that is observed in the central Arctic by the Pathfinder data. Interestingly, we see in Fig. 4g that the FORM run is better at reproducing the seasonal cycle seen in the Pathfinder data, with a marked reduction of the average ice drift in the summer in comparison to the SKIN run.

2) MOMENTUM TRANSFER TO THE ARCTIC OCEAN

As can be seen in Eq. (1), the oceanic drag, or momentum transfer from the ocean to the ice, is determined from the relative ice–ocean velocity and the ONDC. Giles et al. (2012) established a strong correlation between the spatial patterns of the trend in sea surface height and the trend in the wind field curl providing observational evidence that Ekman transport has driven the storage of freshwater in the Beaufort Gyre between 1995 and 2010. In the same study, it was shown that the wind has been more efficient at spinning up the Beaufort Gyre during the 2000s, suggesting a more efficient mechanism has taken place in the momentum transfer from the atmosphere to the ocean over recent years. One possible cause of this increased transfer resides in the mechanical weakening (Gimbert et al. 2012) and the resulting accelerated dynamics of the sea ice cover observed over this period (Rampal et al. 2011). Another possible cause of the increase in momentum transfer lies in changes in the ONDC. In Figs. 5k–t and 6k–t, we show the trend in the ANDC and ONDC as well as their relative contributions in March and August. In both months, we find an increase of the ANDC and ONDC in the Beaufort region accompanied by

a decrease along the west coast of the Arctic Ocean. In March the trend is dominated by the contribution from the ridges, while in the summer (strongest signal in August) the trend is dominated by the floe edge contribution. The overall effect integrated over the year is to increase significantly the drag coefficients and particularly the ONDC in the Beaufort Sea. The trend in recent years of the ONDC appears therefore in addition to the trend in the sea ice drift, as a strong candidate to explain the suggested increase in the coupling between the atmosphere and the ocean.

To account for these two effects jointly and estimate directly their contribution to Ekman pumping (Gill 1982; McPhee 2008), we calculate the curl of the total oceanic stress $\nabla \times \boldsymbol{\tau}$, where the total oceanic drag is the ice area–weighted average of the ice–ocean drag $\boldsymbol{\tau}_w$ and atmosphere–ocean drag $\boldsymbol{\tau}_{\rm wa}$:

$$\boldsymbol{\tau}_w = \rho_w C_{\rm dw} U(\cos\theta \mathbf{U} + \sin\theta \mathbf{k} \times \mathbf{U}) \quad \text{and}$$
$$\boldsymbol{\tau}_{\rm wa} = \rho_w \left(\frac{2.7 \times 10^{-3}}{W} + 1.42 \times 10^{-4} + 7.64 \times 10^{-5} W\right) W^2, \tag{28}$$

where W is the wind velocity magnitude, and we use for the atmosphere–ocean drag coefficient the default parameterization in CICE (Hunke 2010). As in most cases, the concentration of sea ice in the Arctic is very high; the direct contribution from the atmosphere to the ocean can be neglected for climatologies. Nevertheless, when looking at trends in the total oceanic stress, the change in the ice concentration means that this second term can become important. Figures 10a and 10b show the climatologies over the period 1990–2012 of the curl of the total stress $\nabla \times \boldsymbol{\tau}$ for the reference SKIN and FORM runs, respectively. The general enhanced curl over the Beaufort Sea regions is observed in both model runs (stronger in the FORM run) and is coherent with the findings of Giles et al. (2012) and is also confirmed by the general negative vorticity of the sea ice drift (see, e.g., Kwok and Sulsky 2010). The impact of the new form drag formulation becomes clearer when we look at the trend of $\nabla \times \boldsymbol{\tau}$ over the same period for the SKIN run (Fig. 10c) and the FORM run (Fig. 10d). We find that in the run accounting for form drag, the increase in $\nabla \times \boldsymbol{\tau}$ is significant over the Beaufort Sea area (also over the Fram Strait) and could help explain the observed increased momentum transfer in this region.

5. Sensitivity study

The reference run FORM was selected from a procedure of nested sensitivity analysis described in the supplemental materials of this manuscript (available at the Journals Online website at http://dx.doi.org/10.1175/JPO-D-13-0215s1.pdf and http://dx.doi.org/10.1175/JPO-D-13-0215s2.tex), where by modifying the parameters of the models associated with the ridging process we produced a run satisfying $\langle \overline{C}_{\rm da} \rangle = C_{\rm da}^{\rm SKIN}$ and $\langle \overline{C}_{\rm dw} \rangle = C_{\rm dw}^{\rm SKIN}$, while maintaining realistic average values for the sail and keel height and frequency. Here, as summarized in Table 3, we test the sensitivity of the reference FORM run to modifications of relevant parameters of the model. We first modify the local form drag coefficients associated with sails ($c_{\rm ra}$, $c_{\rm kw}$), floe ($c_{\rm fa}$, $c_{\rm dw}$) and melt pond ($c_{\rm pa}$) edges, and skin drag ($c_{\rm sa}$, $c_{\rm sw}$) around their reference values in the FORM run and assess the sensitivity of the reference model to these changes.

As on average, the form drag contribution from sails and keels are the largest to the ANDC and ONDC; modifying the parameters that set their relative magnitude $c_{\rm ra}$ and $c_{\rm kw}$ will most strongly affect the Arctic sea ice characteristics. Indeed, we find that increasing (decreasing) both coefficients simultaneously from $c_{\rm ra} = c_{\rm kw} = 0.2$ to $=0.3$ (0.1) produces a 6.2% increase (1.6% decrease) of the total average ice volume, a small increase (decrease) of the total ice area in the summer season (not shown), and leaves the spatially averaged climatological ice speed over the entire Arctic Basin largely unaffected. In reality, two tendencies are opposing and cancelling out, and the result of increasing these coefficients is to increase (decrease) the ice speed over most of the western (eastern) part of the Arctic Ocean, where the ice becomes more free drift–like. These results are compatible with the early results from Hibler (1979), which showed that increasing the compressive ice strength reduced the overall ice thickness and ice thickness spatial variations while leaving the average ice speed and outflows unchanged. Increasing the effect of the drag terms in the momentum balance has a qualitatively similar effect to reducing the relative contribution from the internal stresses, which is proportional to the compressive strength of the ice.

As can be seen from Table 3, this argument breaks down if only one local form drag coefficient is modified, as the resulting ratio of the ANDC and ONDC $C_{\rm da}/C_{\rm dw}$ is then modified, affecting the relative contributions of ANDC and ONDC in the momentum balance and therefore modifying the ice redistribution over the Arctic. In practice, increasing $c_{\rm sa}$ results in a large increase (~33%) of the average ice speed accompanied by an ice thickness increase concentrating mostly along the western boundary of the Arctic Ocean and along the east Siberian coast as well as by a slight compression of the total ice area, mostly due to a depletion of ice in the east Arctic and in the Fram Strait. Increasing $c_{\rm kw}$ results

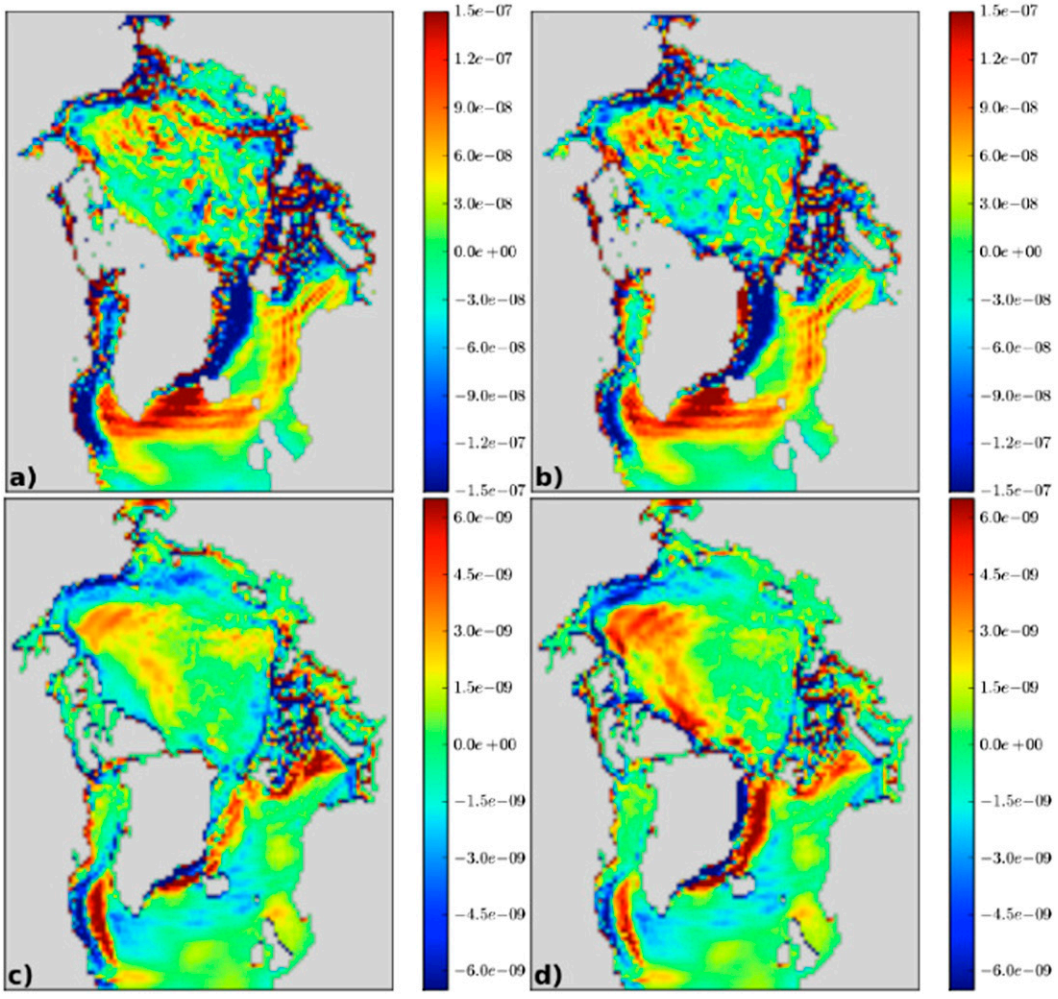

FIG. 10. Climatology over the period 1990–2012 and averaged over all months of the curl of the total oceanic stress for the (a) SKIN and (b) FORM runs. Trend over the same period of the curl of the total oceanic stress for the (c) SKIN and (d) FORM runs. The units are $\mathrm{N\,m^{-3}}$ for (a) and (b) and $\mathrm{N\,m^{-3}\,yr^{-1}}$ for (c) and (d). Note also the convention that the oceanic stress is the force applied from the ocean to the ice.

in approximately the reverse effects on the Arctic sea ice state (reduced thickness, reduced ice speed, and increased ice area). An important difference is that while an increase in c_{sa} results in an increase of ridge formation reflected by a higher sail and keel frequency, and therefore results in an increase in both ANDC and ONDC, an increase of c_{kw}, on the other hand, only modifies the ONDC. These observations are important when considering the influence of the presence of an ocean current in the model (not shown).

Modifying in the same manner the coefficients associated with the local form drag at the floe edges c_{fa} and c_{fw} results in similar trends albeit confined to the MIZ in the winter and in regions where the ice concentration has dropped significantly in the summer season. These parameters are therefore crucial in determining the ice state and dynamics in these regions of lower ice concentration. We expect this contribution to play an increasingly important role in the Arctic as sea ice is becoming more and more of a first-year type and the observed ice concentrations are dropping.

As discussed in section 2, the unobstructed skin drag coefficients c_{sa} and c_{sw} are poorly constrained from observations for both the ice–air and ice–ocean interfaces, and therefore the impact of varying these coefficients in the new drag laws must be tested. To understand how the modification of these parameters affects the total ANDC and ONDC, it is helpful to recognize that the skin contribution to the total drag terms is coupled to the amount of ridging due to the associated sheltering effect. Equations (18) and (19) quantify this effect, making use of the additional free parameters m_a and m_w. Increasing

c_{sa}, as a direct impact, raises the average ANDC, but also indirectly raises the ONDC through additional ridge building. The former increase dominates leading to an increased C_{da}/C_{dw} ratio and hence, as discussed above, an increase of the total volume of ice and average ice speed. For small values of c_{sa}, increasing c_{sw}, on the other hand, leads to the exclusive increase of the ONDC, therefore increasing the ratio C_{dw}/C_{da}. For larger values of c_{sa}, the effect is reversed, as an increase of c_{sw} leads to a small decrease of the ONDC and ANDC due to a reduction of sail and keel formation. The impact of modifying the parameters m_a and m_w remains quite small. Similarly, the impact of the local from drag coefficient associated with the melt pond edges c_{pa} is restricted to the melt season and therefore has only a weak impact on average sea ice characteristics.

Finally, we have also tested the impact of the floe size parameterization, described in Eq. (13) (not shown), and found as expected that the floe size plays an important role in the low ice concentration regions, but only modifies significantly the average sea ice characteristics for unrealistically small average floe sizes. We expect that this effect could be more relevant in the Antarctic where ice floes have been shown to be significantly smaller.

In summary, the results of this sensitivity study show that modifying the relevant parameters of the model within a physically realistic range results in a wide range of possible values of the average ANDC ($0.70 \times 10^{-3} \leq \langle \overline{C}_{da} \rangle \leq 1.95 \times 10^{-3}$) and average ONDC ($4.02 \times 10^{-3} \leq \langle \overline{C}_{dw} \rangle \leq 7.89 \times 10^{-3}$) (see Table 3). The impact of varying the ANDC and ONDC on the sea ice characteristics is illustrated in the plots of Fig. 4, with the shaded areas that correspond to the range of values that the total sea ice extent, volume, and average sea ice drift can take for the range of parameters that we have tested. The uncertainty of the model reflects the necessity to constrain further the parameters of the model against existing and additional observations.

6. Summary and concluding remarks

We have formulated a new, and more physically realistic, model of the atmospheric and oceanic drag terms over the sea ice cover. This new model is largely based on existing theory, which we have collated and implemented into the latest official release (version 5.0) of the stand-alone sea ice model CICE that is used, for example, in the Community Climate System Model (CCSM) and the Met Office Hadley Centre and can therefore easily be tested in coupled climate simulation. We deduce the total neutral form drag coefficients from parameters of the ice cover such as ice concentration, size, and frequency of the sails and keels, freeboard and floe draft, and size of floes and melt ponds. This enables us to isolate four distinct contributions to the total neutral drag, namely form drag from sails and keels, form drag from floe edges, form drag from melt pond edges, and a reduced skin drag due to a sheltering effect. A major improvement over the earlier sea ice models is that the resulting atmospheric and oceanic neutral drag coefficients (ANDC and ONDC) are coupled to the sea ice characteristics and can evolve spatially and temporally.

In the winter, the main contribution to the total drag comes from the heavily ridged regions on the west boundary of the Arctic Ocean, while in the summer, as the sea ice concentration drops, the contribution from floe and melt pond edges becomes significant, and we reproduce the recently observed increase of the drag coefficients during that season (Andreas et al. 2010). The implementation process is straightforward and computationally efficient, with the new form drag model taking the form of a module that can be switched on or off.

While the aim of this paper was not to calibrate the new parameterization to fit observations, it appears that the proposed model performs well in estimating realistic ANDC and ONDC and in reproducing the observed ice concentration, ice thickness, and ice drift temporal and spatial patterns over the Arctic. In our approach we kept the averages of the ANDC and ONDC equal in both runs, even though this reduces the apparent impact of the new physics. In other words, if we compared two models with different average ANDC and ONDC, it would be difficult to disentangle the direct influence of the differing neutral drag coefficients from the impact of the form drag itself. We find that, all other things being equal, introducing the form drag parameterization produces a small average ice thickness, ice area, and ice speed decrease over the Arctic Basin, but more importantly the new model introduces significant spatial and temporal differences with respect to the default model with constant drag coefficients in the distribution of these quantities over the Arctic Ocean, with the most noticeable being a depletion of ice over the west boundary of the Arctic Ocean and over the Beaufort Sea. The new drag parameterization also results in an enhanced positive trend in the curl of the oceanic drag and could explain the increase in sea surface elevation in the Beaufort Sea (Giles et al. 2012).

We have presented a sensitivity study indicating how the free parameters of the new model influence the sea ice behavior. To keep the model as simple as possible, we considered these parameters to be constant in space

and time. The uncertainty of the free parameters of the model calls for a thorough calibration of the new formulation against additional observations of the Arctic sea ice geometrical characteristics (IceBridge) and against measurements of the neutral drag coefficients with an emphasis on the ice–ocean interface. Furthermore comparison of the model predictions against forthcoming ice thickness map measurements extending to high latitudes over the polar regions from *CryoSat-2* appears as an exciting extension of this work. Another important extension of this work will consist in testing the model in the coupled sea ice ocean simulations at higher resolutions. We expect that the new formulation of friction at the sea ice surfaces (top and bottom) will affect the atmospheric boundary layer as well as the heat and momentum exchanges with the ocean and therefore affect the properties of the shallow mixed layer in the Arctic. Finally, an important application of the new model would reside in its application in the Antarctic where the lower sea ice concentration and the reduced roughness of the ice should produce significantly different drag coefficients.

Acknowledgments. We dedicate this paper to our dear, late colleague Prof. Seymour Laxon, who died in tragic circumstances aged 49 on 2 January 2013. Your enthusiasm, dedication, and support were invaluable and a marvel. We miss you sorely.

REFERENCES

Andreas, E. L, T. Horst, A. Grachev, P. Persson, C. Fairall, P. Guest, and R. Jordan, 2010: Parametrizing turbulent exchange over summer sea ice and the marginal ice zone. *Quart. J. Roy. Meteor. Soc.,* **136,** 927–943, doi:10.1002/qj.618.

Arya, S. P. S., 1973: Contribution of form drag on pressure ridges to the air stress on Arctic ice. *J. Geophys. Res.,* **78,** 7092–7099, doi:10.1029/JC078i030p07092.

——, 1975: A drag partition theory for determining the large-scale roughness parameter and wind stress on the Arctic pack ice. *J. Geophys. Res.,* **80,** 3447–3454, doi:10.1029/JC080i024p03447.

Birnbaum, G., and C. Lüpkes, 2002: A new parameterization of surface drag in the marginal sea ice zone. *Tellus,* **54A,** 107–123, doi:10.1034/j.1600-0870.2002.00243.x.

Claussen, M., 1990: Area-averaging of surface fluxes in a neutrally stratified, horizontally inhomogeneous atmospheric boundary layer. *Atmos. Environ.,* **24A,** 1349–1360, doi:10.1016/0960-1686(90)90041-K.

Coon, M., R. Kwok, G. Levy, M. Pruis, H. Schreyer, and D. Sulsky, 2007: Arctic Ice Dynamics Joint Experiment (AIDJEX) assumptions revisited and found inadequate. *J. Geophys. Res.,* **112,** C11S90, doi:10.1029/2005JC003393.

Eicken, H., T. C. Grenfell, D. K. Perovich, J. A. Richter-Menge, and K. Frey, 2004: Hydraulic controls of summer Arctic pack ice albedo. *J. Geophys. Res.,* **109,** C08007, doi:10.1029/2003JC001989.

Farrell, S., and Coauthors, 2012: A first assessment of IceBridge snow and ice thickness data over Arctic sea ice. *IEEE Trans. Geosci. Remote Sens.,* **50,** 2098–2111, doi:10.1109/TGRS.2011.2170843.

Feltham, D., 2008: Sea ice rheology. *Annu. Rev. Fluid Mech.,* **40,** 91–112, doi:10.1146/annurev.fluid.40.111406.102151.

Ferry, N., S. Masina, A. Storto, K. Haines, M. Valdivieso, B. Barnier, and J.-M. Molines, 2011: Product user manual global-reanalysis-phys-001-004. MyOcean Tech. Rep., 30 pp.

Fetterer, F., and N. Untersteiner, 1998: Observations of melt ponds on Arctic sea ice. *J. Geophys. Res.,* **103** (C11), 24 821–24 835, doi:10.1029/98JC02034.

Fissel, D., J. R. Marko, and H. Melling, 2004: Upward looking ice profiler sonar instruments for ice thickness and topography measurements. *Oceans '04: MTTS/IEEE Techno-Ocean '04,* **3,** 1638–1643, doi:10.1109/OCEANS.2004.1406369.

Flato, G., and W. Hibler III, 1995: Ridging and strength in modeling the thickness distribution of Arctic sea ice. *J. Geophys. Res.,* **100** (C9), 18 611–18 626, doi:10.1029/95JC02091.

Flocco, D., and D. L. Feltham, 2007: A continuum model of melt pond evolution on Arctic sea ice. *J. Geophys. Res.,* **112,** C08016, doi:10.1029/2006JC003836.

——, ——, and A. K. Turner, 2010: Incorporation of a physically based melt pond scheme into the sea ice component of a climate model. *J. Geophys. Res.,* **115,** C08012, doi:10.1029/2009JC005568.

——, D. Schroeder, D. L. Feltham, and E. C. Hunke, 2012: Impact of melt ponds on Arctic sea ice simulations from 1990 to 2007. *J. Geophys. Res.,* **117,** C09032, doi:10.1029/2012JC008195.

Fowler, C., 2003: Polar Pathfinder daily 25 km EASE-grid sea ice motion vectors, version 2. National Snow and Ice Data Center, Boulder, CO, digital media. [Available online at http://nsidc.org/data/nsidc-0116.html.]

Garbrecht, T., C. Lüpkes, E. Augstein, and C. Wamser, 1999: Influence of a sea ice ridge on low-level airflow. *J. Geophys. Res.,* **104** (D20), 24 499–24 507, doi:10.1029/1999JD900488.

Giles, K. A., S. W. Laxon, A. L. Ridout, D. J. Wingham, and S. Bacon, 2012: Western Arctic Ocean freshwater storage increased by wind-driven spin-up of the Beaufort Gyre. *Nat. Geosci.,* **5,** 194–197, doi:10.1038/ngeo1379.

Gill, A. E., 1982: *Atmosphere–Ocean Dynamics.* Vol. 30. Academic Press, 662 pp.

Gimbert, F., N. C. Jourdain, D. Marsan, J. Weiss, and B. Barnier, 2012: Recent mechanical weakening of the Arctic sea ice cover as revealed from larger inertial oscillations. *J. Geophys. Res.,* **117,** C00J12, doi:10.1029/2011JC007633.

Guest, P. S., and K. L. Davidson, 1991: The aerodynamic roughness of different types of sea ice. *J. Geophys. Res.,* **96** (C3), 4709–4721, doi:10.1029/90JC02261.

Haas, C., 2004: EM ice thickness measurements during GreenICE 2004 field campaign. AWI Tech Rep. GreenICE Deliverable D11, 24 pp.

——, J. Lobach, S. Hendricks, L. Rabenstein, and A. Pfaffling, 2009: Helicopter-borne measurements of sea ice thickness, using a small and lightweight, digital EM system. *J. Appl. Geophys.,* **67,** 234–241, doi:10.1016/j.jappgeo.2008.05.005.

Hanssen-Bauer, I., and Y. T. Gjessing, 1988: Observations and model calculations of aerodynamic drag on sea ice in the Fram Strait. *Tellus,* **40A,** 151–161, doi:10.1111/j.1600-0870.1988.tb00413.x.

Hartmann, J., C. Kottmeier, and C. Wamser, 1992: *Radiation and Eddy Flux Experiment, 1991 (REFLEX 1).* Berichte zur Polarforschung Series, Vol. 105, Alfred-Wegner-Institut, 72 pp.

Hibler, W., III, 1979: A dynamic thermodynamic sea ice model. *J. Phys. Oceanogr.,* **9,** 815–846, doi:10.1175/1520-0485(1979)009<0815:ADTSIM>2.0.CO;2.

——, 1980: Modeling a variable thickness sea ice cover. *Mon. Wea. Rev.,* **108** (12), 1943–1973, doi:10.1175/1520-0493(1980)108<1943:MAVTSI>2.0.CO;2.

Hunke, E. C., 2010: Thickness sensitivities in the CICE sea ice model. *Ocean Modell.,* **34,** 137–149, doi:10.1016/j.ocemod.2010.05.004.

——, and W. H. Lipscomb, 2010: CICE: The Los Alamos sea ice model documentation and software user's manual version 4.1. Los Alamos National Laboratory Tech. Rep. LA-CC-06-012, 76 pp.

Kalnay, E., and Coauthors, 1996: The NCEP/NCAR 40-Year Reanalysis Project. *Bull. Amer. Meteor. Soc.,* **77,** 437–471, doi:10.1175/1520-0477(1996)077<0437:TNYRP>2.0.CO;2.

Kauffman, B., and W. Large, 2002: The CCSM coupler version 5.01: Combined user's guide, source code reference, and scientific description. National Center for Atmospheric Research Tech. Rep., 47 pp.

Kottmeier, C., J. Hartmann, C. Wamser, A. Bochert, C. Freese, and W. Cohrs, 1994: *Radiation and Eddy Flux Experiment 1993 (REFLEX II).* Berichte zur Polarforschung Series, Vol. 133, Alfred-Wegner-Institut, 62 pp.

Kwok, R., and D. Sulsky, 2010: Arctic Ocean sea ice thickness and kinematics: Satellite retrievals and modeling. *Oceanography,* **23,** 134–143, doi:10.5670/oceanog.2010.11.

Laxon, S. W., and Coauthors, 2013: *CryoSat-2* estimates of Arctic sea ice thickness and volume. *Geophys. Res. Lett.,* **40,** 732–737, doi:10.1002/grl.50193.

Le, H., P. Moin, and J. Kim, 1997: Direct numerical simulation of turbulent flow over a backward-facing step. *J. Fluid Mech.,* **330,** 349–374, doi:10.1017/S0022112096003941.

Leonardi, S., P. Orlandi, R. J. Smalley, L. Djenidi, and R. A. Antonia, 2003: Direct numerical simulations of turbulent channel flow with transverse square bars on one wall. *J. Fluid Mech.,* **491,** 229–238, doi:10.1017/S0022112003005500.

Leppäranta, M., 2005: *The Drift of Sea Ice.* Springer Verlag, 266 pp.

Lipscomb, W., E. Hunke, W. Maslowski, and J. Jakacki, 2007: Ridging, strength, and stability in high-resolution sea ice models. *J. Geophys. Res.,* **112,** C03S91, doi:10.1029/2005JC003355.

López, S., C. Lupkes, and K. Schlunzen, 2005: The effect of different *k*-closures on the results of a micro-scale model for the flow in the obstacle layer. *Meteor. Z.,* **14,** 839–848, doi:10.1127/0941-2948/2005/0084.

Lu, P., Z. Li, B. Cheng, and M. Leppranta, 2011: A parameterization of the ice–ocean drag coefficient. *J. Geophys. Res.,* **116,** C07019, doi:10.1029/2010JC006878.

Lüpkes, C., and G. Birnbaum, 2005: Surface drag in the Arctic marginal sea-ice zone: A comparison of different parameterisation concepts. *Bound.-Layer Meteor.,* **117,** 179–211, doi:10.1007/s10546-005-1445-8.

——, V. M. Gryanik, J. Hartmann, and E. L Andreas, 2012: A parametrization, based on sea ice morphology, of the neutral atmospheric drag coefficients for weather prediction and climate models. *J. Geophys. Res.,* **117,** D13112, doi:10.1029/2012JD017630.

——, ——, A. Rösel, G. Birnbaum, and L. Kaleschke, 2013: Effect of sea ice morphology during Arctic summer on atmospheric drag coefficients used in climate models. *Geophys. Res. Lett.,* **40,** 446–451, doi:10.1002/grl.50081.

Mai, S., C. Wamser, and C. Kottmeier, 1996: Geometric and aerodynamic roughness of sea ice. *Bound.-Layer Meteor.,* **77,** 233–248, doi:10.1007/BF00123526.

Martin, T., 2007: Arctic sea ice dynamics: Drift and ridging in numerical models and observations. Ph.D. thesis, Universität Bremen, 240 pp.

——, and R. Gerdes, 2007: Sea ice drift variability in Arctic Ocean Model Intercomparison Project models and observations. *J. Geophys. Res.,* **112,** C04S10, doi:10.1029/2006JC003617.

McPhee, M. G., 2008: *Air–Ice–Ocean Interaction.* Springer, 216 pp.

——, 2012: Advances in understanding ice–ocean stress during and since AIDJEX. *Cold Reg. Sci. Technol.,* **76–77,** 24–36, doi:10.1016/j.coldregions.2011.05.001.

Melling, H., P. H. Johnston, and D. A. Riedel, 1995: Measurements of the underside topography of sea ice by moored subsea sonar. *J. Atmos. Oceanic Technol.,* **12,** 589–602, doi:10.1175/1520-0426(1995)012<0589:MOTUTO>2.0.CO;2.

Nägeli, W., 1946: Further investigation of the wind conditions in areas with shelterbelts. *Mitt. Schweiz. Anst. Fortstl.,* **24,** 659–737.

Pite, H. D., D. R. Topham, and B. J. van Hardenberg, 1995: Laboratory measurements of the drag force on a family of two-dimensional ice keel models in a two-layer flow. *J. Phys. Oceanogr.,* **25,** 3008–3031, doi:10.1175/1520-0485(1995)025<3008:LMOTDF>2.0.CO;2.

Plate, E., and C. Lin, 1965: The velocity field downstream from a two-dimensional model hill. Part 2. Tech. Rep. DA AMC-36-039-63-G7, 63 pp.

Rampal, P., J. Weiss, C. Dubois, and J.-M. Campin, 2011: IPCC climate models do not capture Arctic sea ice drift acceleration: Consequences in terms of projected sea ice thinning and decline. *J. Geophys. Res.,* **116,** C00D07, doi:10.1029/2011JC007110.

Rothrock, D., 1975: The energetics of the plastic deformation of pack ice by ridging. *J. Geophys. Res.,* **80** (33), 4514–4519, doi:10.1029/JC080i033p04514.

Schröder, D., T. Vihma, A. Kerber, and B. Brümmer, 2003: On the parameterization of turbulent surface fluxes over heterogeneous sea ice surfaces. *J. Geophys. Res.,* **108,** 3195, doi:10.1029/2002JC001385.

Steele, M., J. H. Morison, and N. Untersteiner, 1989: The partition of air–ice–ocean momentum exchange as a function of ice concentration, roe size, and draft. *J. Geophys. Res.,* **94** (C9), 12 739–12 750, doi:10.1029/JC094iC09p12739.

Steiner, N., M. Harder, and P. Lemke, 1999: Sea-ice roughness and drag coefficients in a dynamic thermodynamic sea-ice model for the arctic. *Tellus,* **51A,** 964–978, doi:10.1034/j.1600-0870.1999.00029.x.

Stroeve, J., M. Serreze, M. Holland, J. Kay, J. Malanik, and A. Barrett, 2012: The Arctic's rapidly shrinking sea ice cover: A research synthesis. *Climatic Change,* **110,** 1005–1027, doi:10.1007/s10584-011-0101-1.

Stull, R. B., 1988: *An Introduction to Boundary Layer Meteorology.* Vol. 13. Springer, 666 pp.

Thorndike, A., D. Rothrock, G. Maykut, and R. Colony, 1975: The thickness distribution of sea ice. *J. Geophys. Res.,* **80** (33), 4501–4513, doi:10.1029/JC080i033p04501.

Tremblay, L., and L. Mysak, 1997: Modeling sea ice as a granular material, including the dilatancy effect. *J. Phys. Oceanogr.,*

27, 2342–2360, doi:10.1175/1520-0485(1997)027<2342:MSIAAG>2.0.CO;2.

Tsamados, M., D. L. Feltham, and A. V. Wilchinsky, 2013: Impact of a new anisotropic rheology on simulations of Arctic sea ice. *J. Geophys. Res. Oceans,* **118,** 91–107, doi:10.1029/2012JC007990.

Vihma, T., 1995: Subgrid parameterization of surface heat and momentum fluxes over polar oceans. *J. Geophys. Res.,* **100** (C11), 22 625–22 646, doi:10.1029/95JC02498.

Wadhams, P., and T. Davy, 1986: On the spacing and draft distributions for pressure ridge keels. *J. Geophys. Res.,* **91** (C9), 10 697–10 708, doi:10.1029/JC091iC09p10697.

——, J. P. Wilkinson, and A. Kaletzky, 2004: Sidescan sonar imagery of the winter marginal ice zone obtained from an AUV. *J. Atmos. Oceanic Technol.,* **21,** 1462–1470, doi:10.1175/1520-0426(2004)021<1462:SSIOTW>2.0.CO;2.

Weiss, J., and D. Marsan, 2004: Scale properties of sea ice deformation and fracturing. *C. R. Phys.,* **5,** 735–751, doi:10.1016/j.crhy.2004.09.005.

Zhang, J., and D. A. Rothrock, 2003: Modeling global sea ice with a thickness and enthalpy distribution model in generalized curvilinear coordinates. *Mon. Wea. Rev.,* **131,** 845–861, doi:10.1175/1520-0493(2003)131<0845:MGSIWA>2.0.CO;2.